

# MIGHTEE-H I: Mass Models and Dark Matter properties

Anastasia A. Ponomareva<sup>1,2\*</sup>, P. E. Mancera Piña<sup>3</sup>, A. A. Vărășteanu<sup>2</sup>, M. Glowacki<sup>4,6</sup>, H. Desmond<sup>7</sup>, M. J. Jarvis<sup>2,8</sup>, T. Yasin<sup>2</sup>, I. Heywood<sup>2,9,10</sup>, N. Maddox<sup>11</sup>, E. A. K. Adams<sup>12,13</sup>, M. Baes<sup>14</sup>, A. Gebek<sup>14</sup>, S. Kurapati<sup>12</sup>, M. Maksymowicz-Maciata<sup>11</sup>, K. A. Oman<sup>15,16</sup>, H. Pan<sup>17,2</sup>, I. Prandoni<sup>18</sup>, S. H. A. Rajohnson<sup>19</sup>, I. Ruffa<sup>20</sup> and K. Spekkens<sup>21</sup>

<sup>1</sup>Centre for Astrophysics Research, School of Physics, Astronomy and Mathematics, University of Hertfordshire, College Lane, Hatfield, AL10 9AB, UK

<sup>2</sup>Oxford Astrophysics, Denys Wilkinson Building, University of Oxford, Keble Rd, Oxford, OX1 3RH, UK

<sup>3</sup>Leiden Observatory, Leiden University, P.O. Box 9513, 2300 RA, Leiden, The Netherlands

<sup>4</sup>Institute for Astronomy, University of Edinburgh, Royal Observatory, Edinburgh, EH9 3HJ, United Kingdom

<sup>6</sup>Inter-University Institute for Data Intensive Astronomy, Department of Astronomy, University of Cape Town, Cape Town, South Africa

<sup>7</sup>Institute of Cosmology & Gravitation, University of Portsmouth, Dennis Sciama Building, Portsmouth, PO1 3FX, UK

<sup>8</sup>Department of Physics and Astronomy, University of the Western Cape, Robert Sobukwe Road, Bellville 7535, South Africa

<sup>9</sup>Centre for Radio Astronomy Techniques and Technologies, Department of Physics and Electronics, Rhodes University, PO Box 94, Makhanda, 6140, South Africa.

<sup>10</sup>South African Radio Astronomy Observatory, 2 Fir Street, Black River Park, Observatory, Cape Town, 7925, South Africa.

<sup>11</sup>School of Physics, H.H. Wills Physics Laboratory, Tyndall Avenue, University of Bristol, Bristol, BS8 1TL, UK

<sup>12</sup>ASTRON, the Netherlands Institute for Radio Astronomy, Oude Hoogeveensedijk 4, 7991 PD Dwingeloo, The Netherlands

<sup>13</sup>Kapteyn Astronomical Institute, PO Box 800, 9700 AV Groningen, The Netherlands

<sup>14</sup>Sterrenkundig Observatorium, Universiteit Gent, Krijgslaan 281 S9, B-9000 Gent, Belgium

<sup>15</sup>Institute for Computational Cosmology, Physics Department, Durham University, South Road, Durham DH1 3LE, United Kingdom

<sup>16</sup>Centre for Extragalactic Astronomy, Physics Department, Durham University, South Road, Durham DH1 3LE, United Kingdom

<sup>17</sup>National Astronomical Observatories, Chinese Academy of Sciences, Beijing 100101, People’s Republic of China

<sup>18</sup>INAF-IRA, Via P. Gobetti 101, 40129, Italy

<sup>19</sup>INAF - Osservatorio Astronomico di Cagliari, Via della Scienza 5, I-09047 Selargius (CA), Italy

<sup>20</sup>INAF, Arcetri Astrophysical Observatory, Largo Enrico Fermi 5, I-50125 Florence, Italy

<sup>21</sup>Department of Physics, Engineering Physics and Astronomy, Queen’s University, Kingston, Ontario, K7L 3N6, Canada

Accepted 2025 XX. Received 2025 XX; in original form 2025 XX

## ABSTRACT

Measuring galaxy rotation curves is critical for inferring the properties of dark-matter haloes in the Lambda Cold Dark Matter (ΛCDM) paradigm. We present HI rotation curves and mass models for 20 galaxies from the MIGHTEE survey. Using extended HI kinematics, we construct resolved mass models that include stellar, gaseous, and dark-matter components. Stellar masses are derived using 3.6 μm imaging under fixed mass-to-light ratio ( $\Upsilon_* = M/L$ ) assumptions and are complemented, for the first time for a HI-selected sample, by spatially resolved  $M/L$ , obtained from multi-wavelength SED fitting. We examine the ratio of baryonic to observed rotation velocity ( $V_{\text{bar}}/V_{\text{obs}}$ ) at the characteristic radius  $R_{2.2}$ . Adopting a fixed  $\Upsilon_* = 0.5 M_{\odot}/L_{\odot}$  yields a clear dependence of  $V_{2.2}/V_{\text{obs}}$  on galaxy luminosity, while adopting  $\Upsilon_* = 0.2 M_{\odot}/L_{\odot}$  substantially weakens this trend. In contrast, the resolved  $M/L$  analysis preserves the luminosity dependence while modifying the stellar contribution on a galaxy-by-galaxy basis, providing a more accurate representation of the underlying relation. We model the dark-matter haloes using Navarro–Frenk–White profiles and find that the different assumptions for a fixed  $M/L$  systematically shift galaxies relative to the theoretical stellar-to-halo mass and baryonic-to-halo mass relations, while the spatially varying  $M/L$  yields the closest agreement with theoretical benchmarks within ΛCDM. We therefore demonstrate that future investigations of the dark matter properties of galaxies using rotation curves need to account for varying  $M/L$  across individual galaxy profiles and between galaxies in order to obtain accurate measurements of the dark matter, and therefore test ΛCDM.

**Key words:** Galaxies: kinematics and dynamics – Galaxies: spiral – dark matter – Galaxies: spiral – scaling relations

\* Email: a.ponomareva2@herts.ac.uk

## 1 INTRODUCTION

Since the seminal discoveries in the late 20th century, which revealed that galaxy rotation curves remain flat at large radii rather than declining as predicted by Keplerian dynamics, it has been strongly suggested that most of the mass in galaxies is not visible (Bosma 1978; Rubin et al. 1978; Bosma 1981). This phenomenon provided compelling evidence for the existence of dark matter (van Albada et al. 1985; Begeman et al. 1991). The study of galaxy rotation curves has since been a cornerstone in understanding the distribution of matter in disc galaxies, as well as the connection between baryons and the dark matter (DM) halo. Rotation curves offer direct insight into the gravitational potential of galaxies, since the observed rotation curve consists of contributions from all dynamical components: stars, gas, and DM. Therefore, studying rotation curves is critical for inferring the presence and properties of DM haloes in the Lambda Cold Dark Matter ( $\Lambda$ CDM) paradigm.

Mass modelling of galaxies, which decomposes the total gravitational potential into contributions from baryonic matter (stars and gas) and DM, is a crucial tool for understanding the structure and dynamics of galaxies (de Blok et al. 2008; Martinsson et al. 2013; Aniyani et al. 2018, 2021). By deconstructing the observed rotation curves into the individual contributions from all dynamic components, we can explore the relative contributions of different galactic components to the overall rotation curve and hence determine the properties of the DM halo (de Blok 2010; Oh et al. 2015; Read et al. 2016a; Mancera Piña et al. 2022b). This type of mass modelling provides insights not only into the DM itself but also the processes that shape galaxy formation and evolution, such as feedback from star formation and active galactic nuclei, which can affect the distribution of both baryons and dark matter within the galaxy (Di Cintio & Lelli 2016; Katz et al. 2017; Marasco et al. 2020; Mancera Piña et al. 2022b).

Dark matter halo models, such as the Navarro-Frenk-White (NFW) profile (Navarro et al. 1996) or feedback-modified profiles (e.g. DC14; Di Cintio et al. 2014 or CORENFW; Read et al. 2016b; Allaert et al. 2017), are essential for simulations and theoretical models of galaxy formation and evolution. These models provide parameterised descriptions of the DM halo structure, which can then be tested against the observed rotation curves. The NFW profile, for example, predicts a cuspy halo with a steep density gradient near the centre, as derived from dark matter-only simulations (Springel et al. 2005; Klypin et al. 2011). However, observed rotation curves, especially in low-mass and low-surface-brightness galaxies, often favour dark matter profiles with shallower inner slopes, implying the presence of DM cores rather than cusps (de Blok et al. 2008; Oh et al. 2015; Mancera Piña et al. 2025). The DC14 or CORENFW model (e.g. Read et al. 2016b,a; Allaert et al. 2017), which incorporates the effects of baryonic feedback processes (such as supernova-driven outflows) on dark matter halos, provides a more accurate fit to the observed data in these cases (Di Cintio & Lelli 2016; Katz et al. 2017). These empirical models are crucial for both interpreting observations and refining the theoretical frameworks of galaxy formation. Testing these models against a broad range of galaxy types and properties allows us to assess how well they capture the complexities of galaxy evolution, and whether they are consistent with  $\Lambda$ CDM predictions.

Understanding the mass distribution of galaxies within their DM halos at  $z \sim 0$  is important for tracing the Universe’s assembly history. Theoretical simulations that include baryonic processes, such as gas outflows and star formation, predict that DM halo structures evolve over time (Di Cintio et al. 2014; Tollet et al. 2016). By comparing mass models from observed rotation curves and established DM scaling relations, e.g. the stellar-to-halo mass relation (SHMR) with these simulations, we can evaluate their accuracy and refine our understanding of cosmic growth (Katz et al. 2017; Posti et al. 2019; Marasco et al. 2020; Di Teodoro et al. 2023).

To robustly measure these halo profiles, high-quality rotation curves extending into the outer regions are essential. For galactic mass distribution studies, rotation curves derived from neutral atomic hydrogen (HI) have advantages over optical or other cold gas tracers (de Blok et al. 2008; Lelli et al. 2016; Martinsson et al. 2013), because HI discs tend to extend farther into a galaxy’s outskirts than stellar discs (de Blok et al. 2008; Heald et al. 2011). This extensive spatial coverage allows for the mapping of rotational velocities to a larger radii, providing critical insights into the mass distribution where DM dominates the gravitational potential over baryons (Bosma 1978). Furthermore, HI is dynamically cold (with a velocity dispersion of  $\sigma_v \sim 10 \text{ km s}^{-1}$  (Janjamasimananana et al. 2015; Mogotsi et al. 2016; Mancera Piña et al. 2025) and follows nearly circular orbits, making it ideal for reliably tracing the total gravitational potential (Iorio et al. 2017; Mancera Piña et al. 2021). In contrast, optical and CO tracers are confined to the inner regions due to the much more compact distribution of stars and molecular gas, resulting in a less comprehensive view of a galaxy’s mass profile, and tend to be more susceptible to the mass modelling degeneracy, such as e.g. disc-halo degeneracy, (Frank et al. 2016; de Blok et al. 2016; Combes et al. 2019; Balmaverde et al. 2021; Venturi et al. 2021). These advantages make HI rotation curves an indispensable tool for accurate mass modelling in galactic studies.

A significant challenge in mass modelling of observed rotation curves arises from the disc-halo degeneracy, where the contributions of the stellar disc and dark matter halo to the overall gravitational potential can be difficult to disentangle. This degeneracy arises from the difficulty to accurately determine the mass of the stellar disc, particularly since both the disc and halo influence the shape of the rotation curve (Bershady et al. 2010; Aniyani et al. 2018, 2021). Methods to address this issue include using stellar population synthesis models to estimate the mass-to-light ratio ( $\Upsilon_*$ ) of the stellar disc (Schombert et al. 2019, 2022), or applying the maximum or minimum disc hypotheses, which assume that the disc contributes the maximum or minimum amount of mass allowable by the observed rotation curve. Additionally, other techniques, such as measuring the vertical velocity dispersion of stars in the disc, can provide further constraints to break the degeneracy (Bershady et al. 2010; Martinsson et al. 2013; Aniyani et al. 2018, 2021).

In this paper, we present resolved HI rotation curves for a sample of 20 galaxies selected from the MeerKAT International GigaHertz Tiered Extragalactic Exploration (MIGHTEE) HI Data Release (DR) 1 (Heywood et al. 2024) and utilising L2 band spanning a period of approximately one billion years in lookback time ( $0 < z < 0.08$ ). By combining HI observations with ancillary Spitzer photometry and

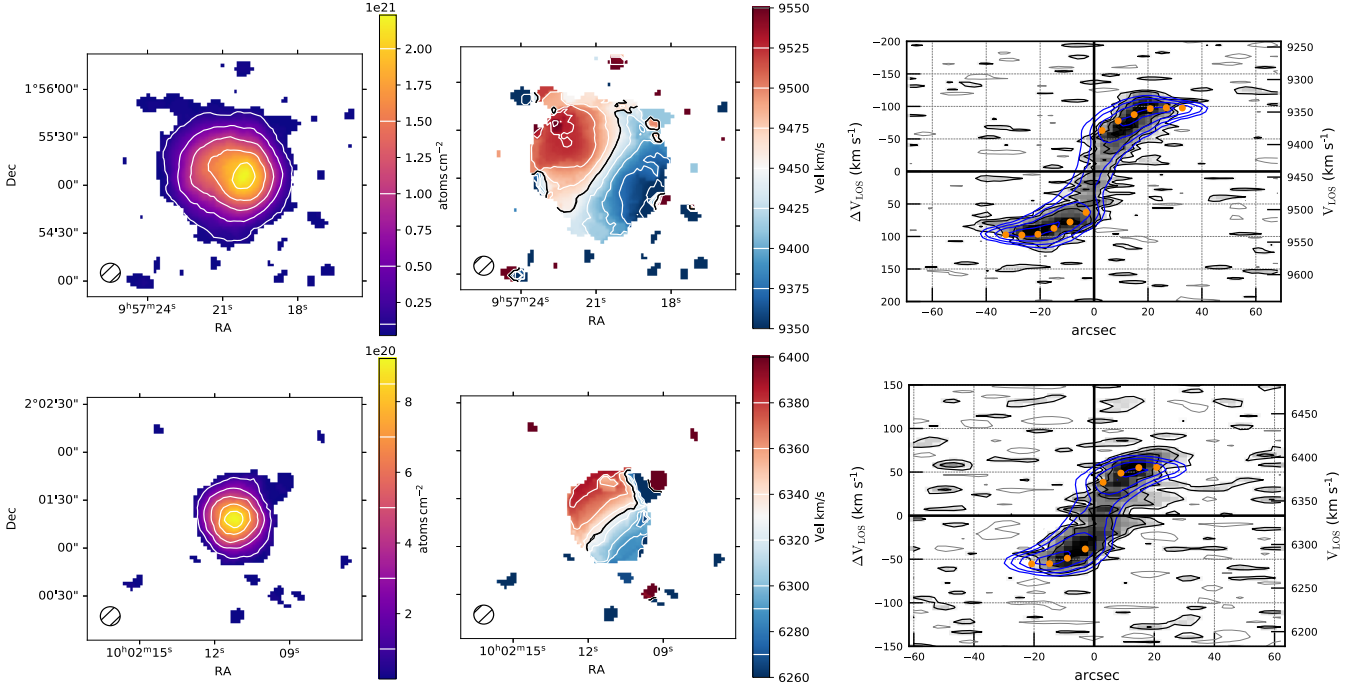


**Figure 1.** HI moment maps and position–velocity (PV) diagrams for two representative galaxies, J095720.6+015507 (top) and J100211.2+020118 (bottom). The left panel shows the HI moment-0 map, the central panel the moment-1 map, and the right panel the position–velocity (PV) diagram along the major axis, with the derived line-of-sight rotation curve (orange) and model (blue) over-plotted. The synthesised beam is shown as an ellipse in the lower left corner.

resolved stellar mass surface densities from Vărășteanu et al. (2025), we construct detailed mass models to disentangle the contributions of stars, gas, and DM in each system. We investigate how different assumptions about stellar mass measurement affect the inferred baryon-to-total dynamic mass relation. We further compare the derived DM halo properties and scaling relations, such as the stellar-to-halo and baryonic-to-halo mass relations, against theoretical predictions from abundance matching and hydrodynamic cosmological simulations.

This paper is organised as follows. Section 2 describes the latest MIGHTEE-HI data release and the HI data utilised in this study. Section 3 explains the derivation of HI rotation curves and surface mass density profiles. Section 4 outlines the method used to obtain stellar brightness profiles. Section 5 presents the constructed mass models and examines the impact of different stellar mass measurements. Section 6 discusses the properties of dark matter and associated scaling relations. Finally, the summary and conclusions, as well as avenues for future work are presented in Section 7.

Throughout the paper we assume a  $\Lambda$ CDM cosmology parameters of  $H_0 = 67.4 \text{ km s}^{-1} \text{ Mpc}^{-1}$ ,  $\Omega_m = 0.315$  and  $\Omega_\Lambda = 0.685$  (Planck Collaboration et al. 2020), and adopt standard values for the critical density ( $\rho_{\text{crit}} = 1.36 \times 10^{11} M_\odot \text{ kpc}^{-3}$ ) and gravitational constant ( $G = 4.3009 \times 10^{-6} \text{ kpc } M_\odot^{-1} (\text{km/s})^2$ ).

## 2 HI DATA

MIGHTEE is a survey of four well-known deep extragalactic fields observed by MeerKAT, the SKA precursor radio inter-

ferometer located in South Africa (Jonas 2009). MeerKAT consists of 64 offset Gregorian dishes (13.5 m diameter main reflector and 3.8 m sub-reflector) and is equipped with three receivers: UHF-band ( $580 < \nu < 1015 \text{ MHz}$ ), L-band ( $900 < \nu < 1670 \text{ MHz}$ ), and S-band ( $1750 < \nu < 3500 \text{ MHz}$ ). The MeerKAT data are collected in spectral mode, making MIGHTEE a spectral line, continuum, and polarisation survey (Jarvis et al. 2016). The HI emission project within the MIGHTEE survey (MIGHTEE-HI) is described in detail in Maddox et al. (2021).

The Early Science (ES) MIGHTEE-HI data have resulted in various publications and discoveries (e.g. Ranchod et al. 2021; Tudorache et al. 2022), with the source catalogue released in Ponomareva et al. (2023). For this study, we utilise the DR1 HI data from the deep MIGHTEE spectral line observations of the COSMOS field (Heywood et al. 2024). These data are deeper and cover a larger area of the COSMOS field than the ES data, with a total of 94.2 h on-target and a close-packed mosaic of 15 individual pointings (covering  $> 4 \text{ deg}^2$  on the sky). The spectral imaging covers two broad regions (960–1150 MHz and 1290–1520 MHz) within MeerKAT’s L-band, with up to 26 kHz ( $5.5 \text{ km s}^{-1}$ ) spectral resolution, in contrast to the ES data with coarser velocity resolution of 208 kHz ( $44 \text{ km s}^{-1}$ ) at  $z = 0$  (Ponomareva et al. 2021).

The data were processed to produce constituent images for mosaics constructed from all pointings at three different resolutions. For this study, we utilise the highest spatial resolution to ensure our galaxies are sufficiently resolved for the 3D kinematic modelling. The typical angular resolution for our data is 12 arcsec with a circular synthesised beam and a velocity resolution of  $5.5 \text{ km s}^{-1}$  at  $z = 0$ . The median noise

in the highest spectral resolution data ( $5.5 \text{ km s}^{-1}$  at  $z = 0$ ) is  $74 \mu\text{Jy beam}^{-1} \text{ channel}^{-1}$ , corresponding to a  $3\sigma$  HI column density sensitivity ( $N_{\text{HI}}$ ) of  $9 \times 10^{18} \text{ cm}^{-2}$ . For a full description of the data processing, analysis, and release, see Heywood et al. (2024).

## 2.1 The Sample

For this study, we rely on the HI source catalogue from the MIGHTEE early science (ES) data covering the COSMOS field (Ponomareva et al. 2023). All 75 galaxies identified in the ES data have been recovered in the DR1 (Heywood et al. 2024). At this stage we do not perform any additional source finding.

Out of the 75 sources, we select galaxies that are resolved with at least three resolution elements across their major axes, as estimated using the  $M_{\text{HI}}-D_{\text{HI}}$  relation (Rajohnson et al. 2022), have inclinations greater than  $20^\circ$ , and are detected in HI with a signal-to-noise ratio exceeding 3 per channel map, ensuring reliable kinematic modelling. For a detailed description of the selection procedure for galaxies suitable for kinematic analysis, see Ponomareva et al. 2021 (Section 4.3.1).

Our final sample comprises 20 galaxies spanning a wide range of circular velocities, from  $40 \text{ km s}^{-1}$  to  $200 \text{ km s}^{-1}$ , HI masses of  $10^7 \leq M_{\text{HI}}[M_\odot] < 10^{10}$  (Heywood et al. 2024), and stellar masses of  $10^7 \leq M_*[M_\odot] < 10^{11}$  (Maddox et al. 2021). The sample spans the entire redshift range of the MIGHTEE L2 band (Heywood et al. 2024), covering approximately 1 Gyr in lookback time ( $0 \leq z \leq 0.08$ ). The HI data (moment 0 and moment 1 maps, as well as position–velocity (PV) diagrams extracted along the major axis) for two representative galaxies from our sample are shown in Figure 1. The main parameters of the sample used in this work can be found in Table A1.

This sample constitutes a pilot study using the MIGHTEE–HI DR1 in the COSMOS field, showcasing the power of the MIGHTEE survey to deliver resolved HI kinematics in deep extragalactic fields up to  $z \sim 0.1$ . Future data releases covering the XMM–Large Scale Structure (XMM-LSS), Extended Chandra Deep Field South (ECDFS), ELAIS-S1 and the MIGHTEE Fornax Survey (MFS) fields will extend this work to hundreds of resolved galaxies.

## 3 HI ROTATION CURVES AND SURFACE MASS DENSITY PROFILES

### 3.1 Rotation curves

Modern 3D kinematic modelling software is capable of constraining gas dynamics in galaxies resolved with as few as three resolution elements across their major axis and with  $\text{SNR} \gtrsim 3$  (Di Teodoro & Fraternali 2015; Kamphuis et al. 2015). Moreover, unlike earlier approaches that required initial estimates of key galactic parameters, such as systemic velocity, central position, and position and inclination angles to derive a rotation curve (Begeman 1989; Verheijen 2001; Ponomareva et al. 2016), modern kinematic modelling software is able to perform fitting procedures with minimal prior information.

In Ponomareva et al. (2021), we explored the capabilities of

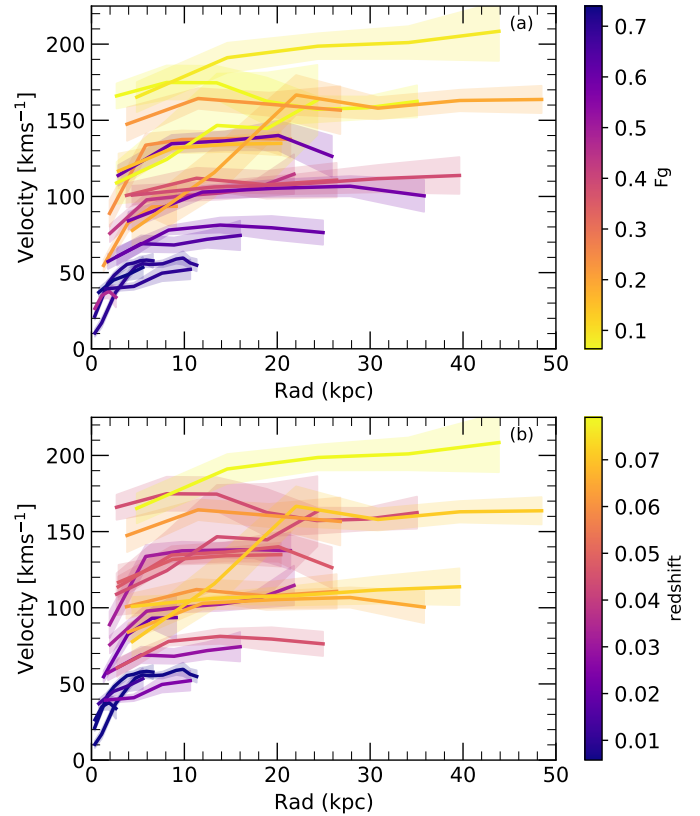


**Figure 2.** Rotation curves of our final sample colour-coded by the galaxies gas fraction  $F_g = M_{\text{HI}}/M_{\text{bar}}$  (a) and by redshift (b). The measurement uncertainties are indicated by the shaded regions

3DBarolo (Di Teodoro & Fraternali 2015) by fitting a sample of sources from the MIGHTEE ES data release in an automated way. Out of the original sample of 270 detections, only 68 presented reliable kinematic measurements suitable for resolved studies, leading to a study of the baryonic Tully–Fisher relation based on resolved kinematics. We have learned that while 3DBarolo is capable of fitting large samples of galaxies in an automated way without prior knowledge of any galaxy parameters, the inclination of galaxies remains a significant issue (Mancera Piña et al. 2020). The software performs much more reliably when an initial estimation of inclination angle is provided (see Figure 2 in Ponomareva et al. 2021).

To derive resolved rotation curves for our sample of galaxies, we use inclinations measured from the Spitzer IRAC 1 band at  $3.6 \mu\text{m}$ , which is widely adopted to trace the bulk of the stellar mass distribution in galaxies (Ponomareva et al. 2017; Querejeta et al. 2015a; Meidt et al. 2012a). This near-infrared band is minimally affected by dust extinction and is largely insensitive to recent star formation, providing a robust representation of the disc geometry.

The inclinations ( $i$ ) are estimated from the axis ratios using the standard relation:

$$\cos^2(i) = \frac{(b/a)^2 - q_0^2}{1 - q_0^2}, \quad (1)$$

where  $b$  and  $a$  are the semi-minor and semi-major axes, respectively, and  $q_0$  represents the intrinsic axis ratio of the disc, typically ranging between 0 (infinitely thin disc) and

0.4 (Fouque et al. 1990). Throughout this work, we adopt a standard value of  $q_0 = 0.2$ , following Tully & Fouque (1985).

We then use these inclinations to run 3DBarolo fully automatically, using only the data cube and the inclination as input values, keeping  $V_{\text{rot}}$  and  $V_{\text{disp}}$  as free parameters. The fully automated run adopts a ring separation equal to the beam major axis, ensuring that the kinematic measurements are largely independent and that pixel-to-pixel correlations remain negligible.<sup>1</sup> We set the boundary constraint for inclination fitting to  $\Delta i = \pm 5^\circ$  (see Ponomareva et al. 2021 for details). To account for the uncertainties on the derived rotation curves and HI surface mass densities we utilise the built-in FLAGERRORS function in 3DBarolo, which estimates the uncertainties on the fitted parameters and the resulting rotational velocities by exploring the full parameter space, ensuring the fit converges at the minima (Di Teodoro & Fraternali 2015).

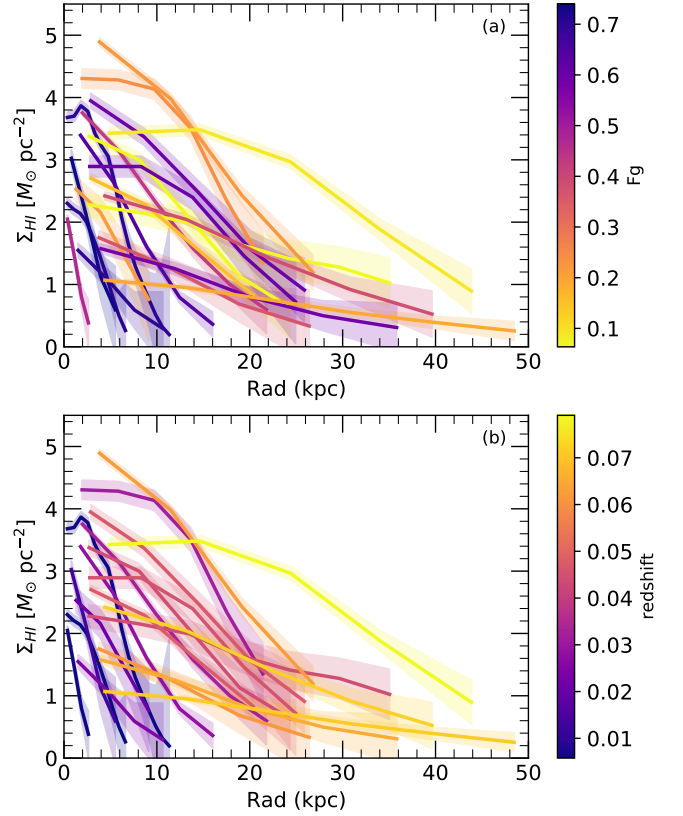
The resulting rotation curves for two representative galaxies from our sample are shown in Figure 1 overplotted on top of the PV diagrams along the major axis. The compilation of all resulting rotation curves is shown in Figure 2. Given the nature of our volume-limited, untargeted survey, it is unsurprising that we predominantly detect gas-rich, low-velocity galaxies at lower redshifts, whereas galaxies with higher stellar masses appear at higher redshifts (due to larger volume probed) and exhibit lower gas fractions:  $F_g = 1.4M_{\text{HI}}/M_{\text{bar}}$ , where  $M_{\text{bar}} = 1.4M_{\text{HI}} + M_*$ , with the factor 1.4 accounting for the primordial abundance of helium and metals (Arnett 1999). We note that our rotation curves are not corrected for pressure support (i.e. we do not apply the asymmetric drift correction, e.g. Binney & Tremaine 2008; Read et al. 2016a; Mancera Piña et al. 2026). This correction is negligible for HI at our mass and rotational speed ranges, and becomes important only for galaxies  $V_{\text{rot}}/\sigma_v \lesssim 3$ , which are typically dwarfs with  $V_{\text{rot}} \lesssim 20 \text{ km s}^{-1}$  (e.g. Iorio et al. 2017; Mancera Piña et al. 2021).

Figure 2 (b) shows the derived rotation curves as a function of redshift. Prior to our study, resolved HI rotation curve samples only covered galaxies up to redshift  $z = 0.02$  (Deg et al. 2022, 2024). Although this redshift range is not expected to encompass any cosmological HI evolution (Ponomareva et al. 2021), it mitigates distance uncertainties arising from the local universe’s cosmic flow and allows for cosmological luminosity distance measurements. The systemic velocities of our sample range from  $V_{\text{sys}} \approx 1700 \text{ km s}^{-1}$  to  $V_{\text{sys}} \approx 22770 \text{ km s}^{-1}$ , with a mean value of  $\bar{V}_{\text{sys}} \approx 11800 \text{ km s}^{-1}$ , making the effect of peculiar velocities negligible for the majority of the sample (Tonry et al. 2000; Tully et al. 2016; Said et al. 2020).

### 3.2 Gas Surface Mass Density

Following the extraction of rotation curves, we also derive resolved radial HI surface mass density profiles taking advantage of 3DBarolo. At each radius, the mean HI flux density is estimated from the input data cubes. We then con-

<sup>1</sup> For consistency and to prepare for the large data load from the ongoing and upcoming HI surveys, we run the fully automated version of 3DBarolo, following the methodology and motivation detailed in Ponomareva et al. (2021).



**Figure 3.** Inclination corrected HI surface mass density 1D profiles of our final sample, colour-coded by the galaxies’ gas fraction  $F_g = M_{\text{HI}}/M_{\text{bar}}$  (a) and by redshift (b). The measurement uncertainties are indicated by the shaded regions.

vert these values from units of flux density to physical units of HI column density,  $N_{\text{HI}}$  [atoms  $\text{cm}^{-2}$ ], following the standard procedure (see Eq. 78 in Meyer et al. 2017). Next, we correct the column density profiles for inclination to obtain face-on values, thereby accounting for projection effects due to the galaxies’ orientation. Finally, we apply the standard conversion to obtain HI surface mass density, where  $1 M_{\odot} \text{ pc}^{-2} = 1.249 \times 10^{20} \text{ atoms cm}^{-2}$ .

The resulting HI surface mass density profiles are shown in Figure 3. As expected, they exhibit a variety of shapes across our sample of galaxies. Higher mass galaxies tend to illustrate a central depletion of HI surface density, with the neutral hydrogen gas extending out to large radii. This indicates that in these galaxies, the HI gas is more distributed in the outer regions of the galactic disc. Conversely, smaller galaxies display steeper HI profiles.

## 4 STELLAR SURFACE BRIGHTNESS AND MASS DENSITIES

### 4.1 Spitzer photometry

The Spitzer IRAC 1 band at  $3.6 \mu\text{m}$  is widely used to derive stellar surface brightness profiles, which are essential for subsequent mass modelling and rotation curve decomposition. One of the key advantages of the  $3.6 \mu\text{m}$  wavelength is its sensitivity to the older, low-mass stars that dominate the

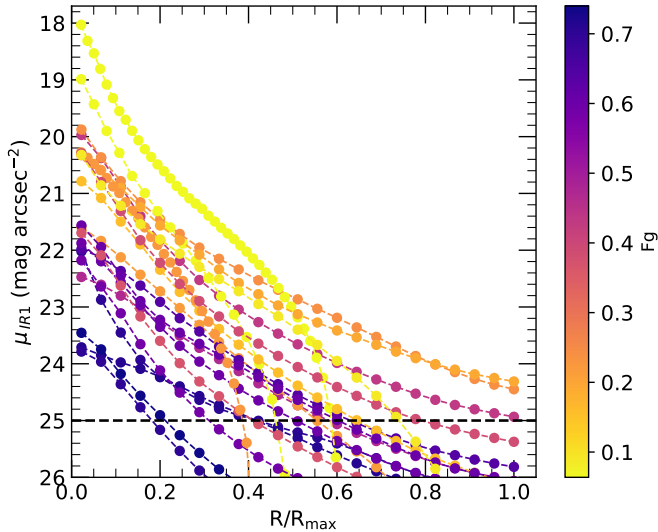


**Figure 4.** IRAC 1 surface brightness profiles of our final sample colour-coded by the galaxies’ gas fraction,  $F_g = M_{\text{HI}}/M_{\text{bar}}$  and normalized by the radius of the last measured ellipse ( $R_{\text{max}}$ ). The horizontal dashed line represents the Spitzer IRAC 1  $3\sigma$  magnitude limit

bulk of the stellar mass in galaxies. At this wavelength, the emission is not affected by dust extinction and is predominantly due to evolved stellar populations such as red giants and main-sequence stars. This results in a more accurate tracing of the underlying stellar mass distribution compared to optical wavelengths, which can be significantly influenced by recent star formation and dust obscuration (Sheth et al. 2010; Meidt et al. 2012b).

Furthermore, the stellar mass-to-light ratio ( $\Upsilon_*$ ) in the  $3.6 \mu\text{m}$  band is considered to be well understood and stable across different galaxy types and stellar populations. Studies have shown that the  $\Upsilon_*$  at  $3.6 \mu\text{m}$  exhibits minimal variation with stellar population age or metallicity (Röck et al. 2015), allowing for a more direct and reliable conversion from observed luminosity to stellar mass (McGaugh & Schombert 2014). Meidt et al. (2014b), for example, showed that the intrinsic scatter in the  $\Upsilon_*$  ratio at  $3.6 \mu\text{m}$  is less than 0.1 dex, which is significantly lower than in optical bands. Marasco et al. (2025) performed a comparison between stellar masses inferred from  $3.6 \mu\text{m}$  data and those derived through multi-wavelength SED modelling, demonstrating that SED fitting provides consistent stellar mass estimates in good agreement with dynamical estimates.

Additionally, the minimal impact of dust extinction at  $3.6 \mu\text{m}$  reduces the need for uncertain extinction corrections, further improving the accuracy of the stellar mass profiles (Querejeta et al. 2015b). This is particularly beneficial for edge-on galaxies or regions with high dust content, where optical observations can be severely affected. The use of  $3.6 \mu\text{m}$  data thus allows for a clearer view of the stellar mass distribution, which is crucial for understanding the interplay between baryonic and dark matter in galaxies (Ponomareva et al. 2017, 2018). Numerous studies have successfully utilised Spitzer IRAC 1 band data for mass modelling and rotation curve decomposition (e.g. McGaugh et al. 2016; Lelli et al. 2016; Posti et al. 2019; Di Teodoro et al. 2023).

Taking all of this into account, for our study we also focus on the Spitzer  $3.6 \mu\text{m}$  band to derive the stellar mass surface density for the sample galaxies. To obtain the stellar surface brightness profiles necessary for mass modelling and rotation curve decomposition, we processed the galaxy images using the standard approach (Vărășteanu et al. 2025) and extracted the stellar surface brightness profile of each galaxy.

We defined a series of concentric elliptical annuli centred on each galaxy, with the separation between annuli set equal to the Spitzer IRAC 1 point spread function (PSF) full width at half maximum (FWHM  $\sim 1.7''$ ). The number of elliptical apertures was left unconstrained and extended to the edge of the image, where the background is well sampled, ensuring that the integrated light converges and the radial surface-brightness profile reaches a flat asymptotic tail. The ellipticity and position angle of the ellipses were fixed to the geometry measured using Eq. 1. Fixing the ellipse geometry, rather than allowing each annulus to follow the isophotal contours, has been shown to be effective for deriving surface-brightness profiles, particularly for  $3.6 \mu\text{m}$  data (Marasco et al. 2023; Siljeg et al. 2024).

Within each annulus, the mean intensity was calculated after correcting for residual background flux and applying aperture corrections. The measurement errors on the mean intensity were computed following the standard photometric error-propagation approach, in which the total variance is the sum of contributions from the object signal, sky background, and readout noise, with background noise dominating the uncertainty at faint levels (Howell 2006). The resulting surface-brightness profiles, corrected for inclination, are shown in Figure 4 for all galaxies in the sample.

## 4.2 Resolved stellar mass surface densities

Owing to the limited wavelength coverage of many HI samples,  $3.6 \mu\text{m}$  imaging has commonly been used as the optimal single-band proxy for stellar mass. However, within the MIGHTEE fields we have access to some of the deepest and high-quality visible (e.g. Aihara et al. 2018, 2019) and near-infrared (e.g. McCracken et al. 2012; Jarvis et al. 2013) imaging data available.

Therefore, in addition to the stellar surface-brightness profiles derived from the Spitzer IRAC 1 ( $3.6 \mu\text{m}$ ) imaging, we incorporate into our analysis the resolved stellar mass surface densities measured by Vărășteanu et al. (2025). These were obtained through spatially resolved spectral energy distribution (SED) fitting across ten optical and near-infrared bands, yielding resolved stellar mass surface-density profiles (see Figure 4 of Vărășteanu et al. 2025).

The Vărășteanu et al. (2025) sample is composed of the same HI-selected galaxies and overlaps with our own sample for 19 out of 20 systems. Their resolved stellar mass measurements therefore provide an independent and complementary dataset that strengthens our characterisation of the stellar mass distribution and its contribution to the baryonic mass budget. Spatially resolved stellar mass surface densities based on radially varying  $\Upsilon_*$  have so far been used for mass modelling and DM inference only in a single-object study (Tamm et al. 2012). Here we extend this approach to a larger sample. Hereafter, we refer to these resolved stellar mass surface-density profiles as the resolved  $\Upsilon_*$  profiles.

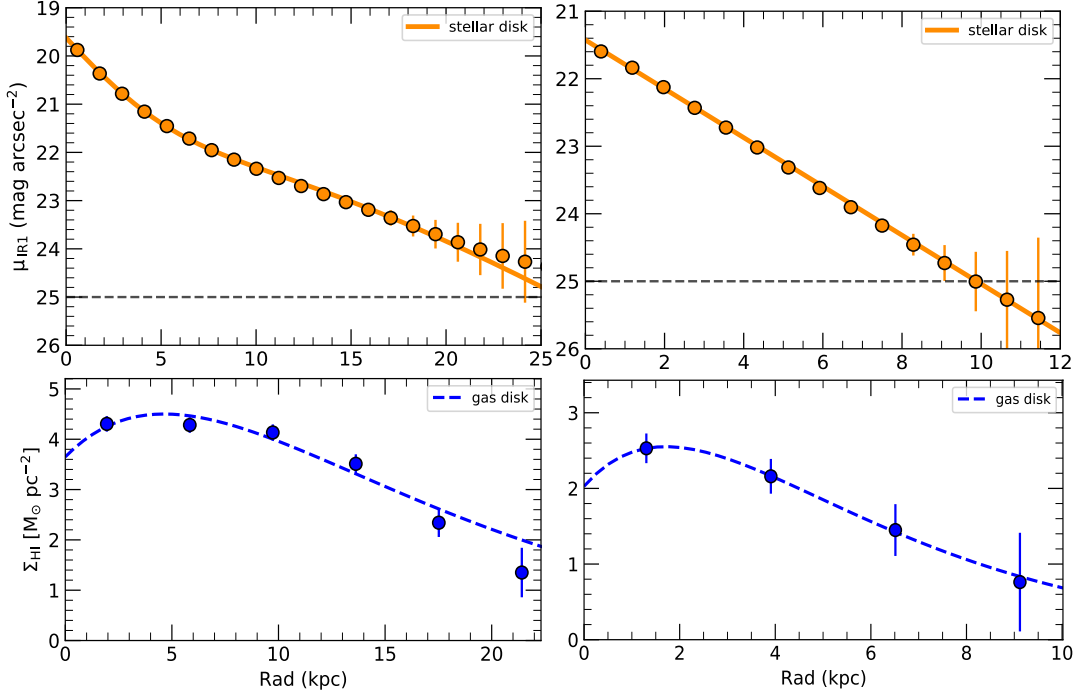


**Figure 5.** Surface brightness and HI gas density profiles for two representative galaxies J095720.6+015507 and J100211.2+020118 from our sample. Left column: Profile for a galaxy with a pseudo bulge (orange points) described by a poly-exponential fit (orange line). The horizontal dashed line represents the  $3\sigma$  magnitude limit. The bottom panel displays the radial profile of the HI gas surface density (blue points), with the dashed blue line representing the poly-exponential gas disc fit and the points indicating the observed data. Right column: Profile for a galaxy without a bulge (orange points), described by exponential disc fit (line), the bottom panel shows the gas surface density profile (blue points) described by the poly-exponential gas disc fit (blue dashed line)

## 5 MASS MODELS

Rotation curve decomposition enables us to separate the contributions from visible and dark matter, offering a comprehensive picture of the overall mass structure within a galaxy. The total rotational velocity  $V_{\text{tot}}(R)$  at a given radius  $R$  can be expressed as the square root of the quadratic sum of the rotational velocities contributed by the various mass components of the galaxy. These components include the baryonic matter comprising gas, bulge and disc ( $V_{\text{bar}}$ ), and the dark matter halo ( $V_{\text{halo}}$ ):

$$V_{\text{tot}}^2(R) = V_{\text{bar}}^2(R) + V_{\text{halo}}^2(R). \quad (2)$$

Analysing the individual contributions of these components allows us to understand the distribution of mass within each one. The gas component  $V_{\text{gas}}(R)$  is derived from the observed HI surface density profile (Section 3.2), while the stellar components  $V_{\text{bulge}}(R)$  and  $V_{\text{disc}}(R)$  are obtained from the surface brightness profiles (Section 4) converted to mass profiles using appropriate mass-to-light ratios. We neglect the contribution from molecular gas, which is expected to have only a minor impact on the mass modelling (Frank et al. 2016; Ponomareva et al. 2018; Mancera Piña et al. 2022b). The DM halo’s contribution  $V_{\text{halo}}(R)$  is modelled to account for any discrepancy between the observed rotation curve (Section 3.1) and the one from the baryonic components:

$$V_{\text{bar}}^2(R) = V_{\text{gas}}^2(R) + V_{\text{stars}}^2(R). \quad (3)$$

We construct our mass models by closely following the

methodology from Mancera Piña et al. (2022a,b). To compute the gas and stellar rotation velocities, we utilise the software GALPYNAMICS<sup>2</sup>, which numerically calculates the gravitational potential of a given mass distribution described by a density profile as a function of radius and height above the disc mid-plane. Subsequently, GALPYNAMICS computes the circular velocity of the mass distribution by taking the derivative of the gravitational potential evaluated at the mid-plane of the mass component (see Section 3.1 in Mancera Piña et al. 2022b for details).

To obtain the functional forms of the density distribution of the baryonic components of our sample galaxies, we first fit the observed HI surface mass density profiles with the poly-exponential function:

$$\Sigma_{\text{HI}}(R) = \Sigma_0 \exp\left(-\frac{R}{R_d}\right) (1 + c_1 R + c_n R^n + \dots), \quad (4)$$

where  $\Sigma_0$  is the central surface mass density,  $R_d$  is the exponential disc scale length, and  $c_1$ ,  $c_2$ ,  $c_n$  etc., are the coefficients of the polynomial. This function closely matches the surface-density profiles of gas-rich galaxies, which commonly show a central plateau or depression, rise at intermediate radii, and decline approximately exponentially at large radii (e.g. Swaters 1999; Wang et al. 2016; Martinsson et al. 2016). For complex, well-resolved data, the number of polynomial coefficients can reach up to four (Mancera Piña et al. 2024).

<sup>2</sup> <https://gitlab.com/iogiul/galpynamics>

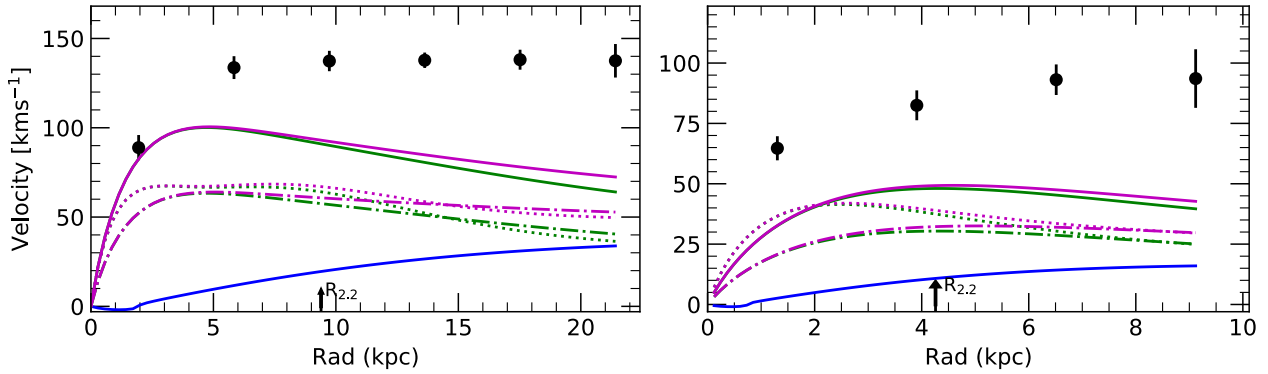


**Figure 6.** Baryonic mass modelling for two representative galaxies J095720.6+015507 and J100211.2+020118 from our sample. Left panel: Mass modelling for the galaxy with poly-exponential disc. The observed rotation curve (black points) is compared with modelled rotational velocities from gas (blue line) and stellar disc (green line). The total baryonic rotation curve  $V_{\text{bar}}$  is shown with a magenta line. Solid lines represent adopted  $\Upsilon_* = 0.5$ , dashed-dotted lines correspond to  $\Upsilon_* = 0.2$  and dotted lines correspond to the SED profiles. The arrow indicates the radius corresponding to 2.2 disc scale lengths. Right panel: Baryonic mass modelling for the galaxy with pure exponential disc

However, for our marginally resolved HI surface mass density profiles, we use only the first-degree coefficient to avoid over-fitting. The resulting fits are shown in Figure 5 (bottom panels) for two representative galaxies from our sample and demonstrate that the chosen functional form can reproduce the data, capturing the central depression common in the HI surface mass density distribution (Ponomareva et al. 2016).

Next, we model the stellar light distribution by fitting the stellar surface brightness profiles (Figure 4) using a functional form. For galaxies with a deviation from the pure exponential disc and excess light in the centre we first model the total intensity as the sum of two components: a bulge, described by a general Sérsic profile:

$$I(R) = I_e \exp \left( -b_n \left[ \left( \frac{R}{R_e} \right)^{1/n} - 1 \right] \right), \quad (5)$$

where  $I_e$  is the intensity at the effective radius  $R_e$ ,  $n$  is the Sérsic index, and  $b_n$  is a constant that depends on  $n$  (Ciotti & Bertin 1999), and a disc, represented by an exponential profile (a Sérsic profile with  $n = 1$ ). We find that none of the bulges in our sample actually represent the classical bulge population, which is typically described with Sérsic index  $n > 2$ . Instead, we find that bulges in our sample are consistent with pseudobulges ( $n \leq 2$ ). Pseudobulges, also known as disc-like bulges, are thought to form through the secular evolution of the galaxy’s disc, driven by internal processes such as bars, spiral arms, and oval distortions (Kormendy & Kennicutt 2004). Therefore, we cannot model the dynamics of these components as purely spherical, like classical bulges. Instead, we fit our stellar profiles that exhibit this feature with a poly-exponential disc of the fourth order (Eq. 4; Mancera Piña et al. 2024). For pure disc systems, we fit only an exponential disc profile. Figure 5 (upper panels) shows examples of these fits for two representative galaxies: one with a pseudobulge and another with a purely exponential disc.

To convert Spitzer intensities to stellar mass surface density, we use the prescription from Lelli et al. (2016). We apply two different values of the  $\Upsilon_*$  for the stellar disc: the traditional value for the  $3.6 \mu\text{m}$  band,  $\Upsilon_* = 0.5$  (Meidt et al. 2014a; Schombert et al. 2019) and  $\Upsilon_* = 0.2$ , found by Mar-

tinsson et al. (2013) for the discMass Survey and by Ponomareva et al. (2018) using SED modelling of disc galaxies over 18 photometric bands. In the following, we examine how different choices of  $\Upsilon_*$  affect the mass modelling and compare these results with those derived from spatially resolved  $\Upsilon_*$  estimates.

We adopt the same functional forms (poly- and exponential disk) to describe the resolved  $\Upsilon_*$  profiles from Vărașteanu et al. (2025), who demonstrated that this form provides an adequate representation of the data.

To account for the stellar disc thicknesses, we adopt the standard assumption that the scale height of the stellar disk is  $\sim 0.1R_d$  (Yoachim & Dalcanton 2006; Comerón et al. 2018). We model the vertical structure of the stellar disc using a  $\text{sech}^2$  density profile (van der Kruit & Freeman 2011). For the gas disc, we assume the razor-thin approximation (Bosma 1981; Wang et al. 2016). While in reality the gas discs flare with radius (e.g. Romeo 1992; Bacchini et al. 2019), the dynamical effect of the flaring is only important for gas-rich dwarf galaxies with  $V_{\text{rot}} \lesssim 30 \text{ km/s}$  and  $V_{\text{rot}}/\sigma_v \lesssim 3$  (Mancera Piña et al. 2022b, 2025), and therefore can be neglected in our sample. Moreover, accurate computation of scale heights requires highly resolved HI observations, which are not yet attainable for samples beyond the very local universe. Therefore, we consider our approximations suitable for our sample and proceed with modelling the dynamics of the baryonic components.

Figure 6 illustrates the baryons-only mass models for two representative galaxies from our sample, with stellar circular velocities computed from the  $3.6 \mu\text{m}$  profiles assuming  $\Upsilon_* = 0.5$  (solid lines) and  $\Upsilon_* = 0.2$  (dash-dotted lines), and from the resolved  $\Upsilon_*$  profiles (dotted lines). From Figure 6, it is clear that for the galaxy with higher rotational velocity, the stellar circular velocity derived from the resolved  $\Upsilon_*$  is closer to that obtained assuming  $\Upsilon_* = 0.2$ , whereas for the galaxy with lower rotational velocity it is closer to the case with  $\Upsilon_* = 0.5$ . This behaviour is consistent with the findings of Vărașteanu et al. (2025), who showed that galaxies do not share a universal stellar mass-to-light ratio, and that  $\Upsilon_*$  varies not only from galaxy to galaxy but also within in-

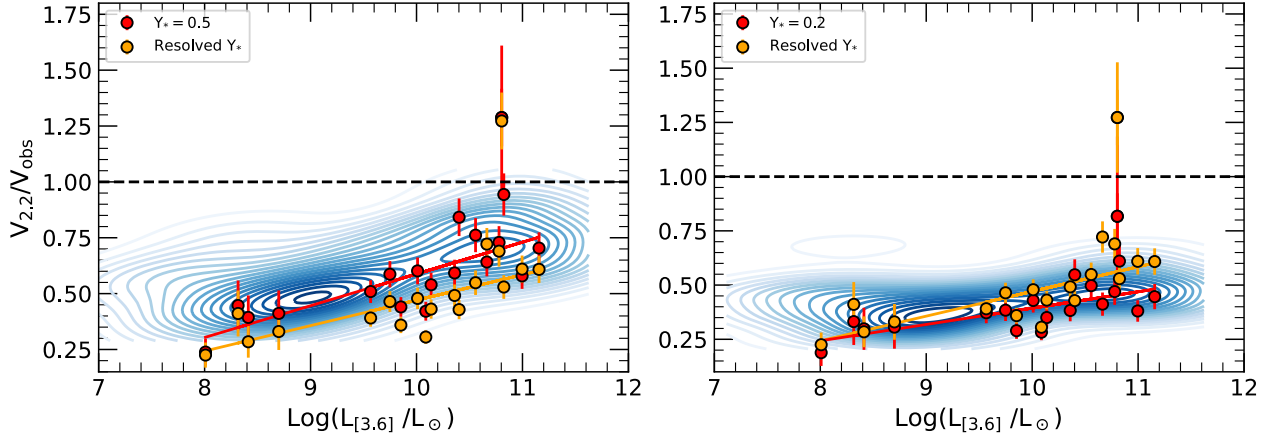


**Figure 7.** Ratio of the baryonic to observed rotation velocity at 2.2 disc scale lengths ( $V_{2.2}/V_{\text{obs}}$ ) as a function of the total luminosity in the  $3.6 \mu\text{m}$  band for our sample galaxies (red points), shown for two adopted values of the stellar mass-to-light ratio  $\Upsilon_*$  (Section 5). Observational trends from the SPARC database (Lelli et al. 2016) are highlighted with blue regions. The dashed line represents  $V_{\text{bar}}/V_{\text{obs}} = 1$ , which marks the upper limit for physically acceptable discs

dividual galaxies as a function of radius (see Figures 6 and 7 in Vărașteanu et al. 2025).

An arrow indicates the radius corresponding to  $2.2 \times R_d$  ( $R_{2.2}$ ) (Freeman 1970). This radius is often used for the mass modelling of galaxies since for an exponential disc, the stellar rotation curve reaches its maximum at  $\sim R_{2.2}$  (van Albada et al. 1985; Binney & Tremaine 2008). The ratio between the rotational velocity of the baryons and the observed rotational velocity at this characteristic radius gives a measure of the degree of the disc “maximality” (Martinsson et al. 2013; Starkman et al. 2018). A “maximal disk” in a spiral galaxy is commonly defined as one in which the stellar disk component contributes the largest fraction of the observed rotation curve ( $\sim 85\% \pm 10\%$  of the peak velocity), while leaving minimal room for a DM halo contribution (van Albada & Sancisi 1986). Figure 6 shows that for the first galaxy (left),  $\Upsilon_* = 0.5$  produces a maximal disc, as any higher  $\Upsilon_*$  would result in a total rotation curve exceeding the observed data. In contrast, the second galaxy (right) demonstrates greater flexibility, allowing for either a larger  $\Upsilon_*$  or a more substantial DM contribution. Adopting  $\Upsilon_* = 0.2$ , on the other hand, results in the discs of both galaxies being submaximal.

### 5.1 The Effect of the Stellar Mass-To-Light Ratio

Figure 7 shows the ratio of the baryonic to observed rotational velocities ( $V_{2.2}/V_{\text{obs}}$ ) measured at  $2.2R_d$  for our sample galaxies, considering three different  $\Upsilon_*$  as described in Section 5.

Firstly, we note that our sample reproduces the same trends found by Lelli et al. (2016) for 175 large nearby disc galaxies (the SPARC sample). We find that the degree of disc maximality depends on the total luminosity of a galaxy when  $\Upsilon_* = 0.5$  is adopted. Figure 7 (left) demonstrates that the values of  $V_{2.2}/V_{\text{obs}}$  increase from approximately 0.25 for faint galaxies to nearly 1 for galaxies with higher total luminosity.

Conversely, this trend almost disappears when  $\Upsilon_* = 0.2$  is adopted (Figure 7, right), signifying little dynamical distinction between galaxies of different luminosities when a low  $\Upsilon_*$  is assumed. However, a scenario in which all spiral galaxies

have uniformly low stellar mass contributions would lead to systematic deviations from the baryonic Tully–Fisher relation (McGaugh et al. 2000) at fixed rotation velocity, which are not observed (Ponomareva et al. 2018, 2021).

Moreover, as demonstrated by Vărașteanu et al. (2025), spatially resolved stellar mass surface densities derived from SED fitting reveal that  $\Upsilon_*$  varies both from galaxy to galaxy and as a function of radius within individual systems. This implies that the stellar contribution to the baryonic mass distribution is neither globally uniform nor radially constant, but instead depends on the specific properties of each galaxy and location within it.

To assess how such non-universal, resolved  $\Upsilon_*$  affects trends in fractional baryonic contribution in the inner regions, we examine their impact on the  $V_{2.2}/V_{\text{obs}}$ –luminosity relation. For this purpose, we fit a linear relation in order to quantify how the slopes of the relations change. We find that when a high stellar mass-to-light ratio ( $\Upsilon_* = 0.5$ ) is assumed, the ratio  $V_{2.2}/V_{\text{obs}}$  increases systematically with luminosity, with a slope of  $0.18 \pm 0.04$ , indicating that more luminous spiral galaxies are increasingly baryon-dominated in their inner regions. Resolved stellar mass surface densities yield a similarly strong luminosity dependence, with a slope of  $0.15 \pm 0.03$ , differing primarily in normalisation (Figure 7, orange). This demonstrates that incorporating spatially resolved stellar mass distributions preserves the physical trend of increasing inner baryonic dominance with luminosity while refining the stellar mass contribution on a galaxy-by-galaxy basis. In contrast, adopting a low stellar mass-to-light ratio ( $\Upsilon_* = 0.2$ ) tends to reduce the baryonic contribution at  $2.2R_d$  across the full luminosity range, leading to an almost flat relation with a slope of only  $0.05 \pm 0.03$ .

Therefore, the resolved stellar mass estimates preserve a physically meaningful  $V_{2.2}/V_{\text{obs}}$  dependence on luminosity, as well as alleviate the extreme form of the disc–halo degeneracy introduced by assuming a single  $\Upsilon_*$ .

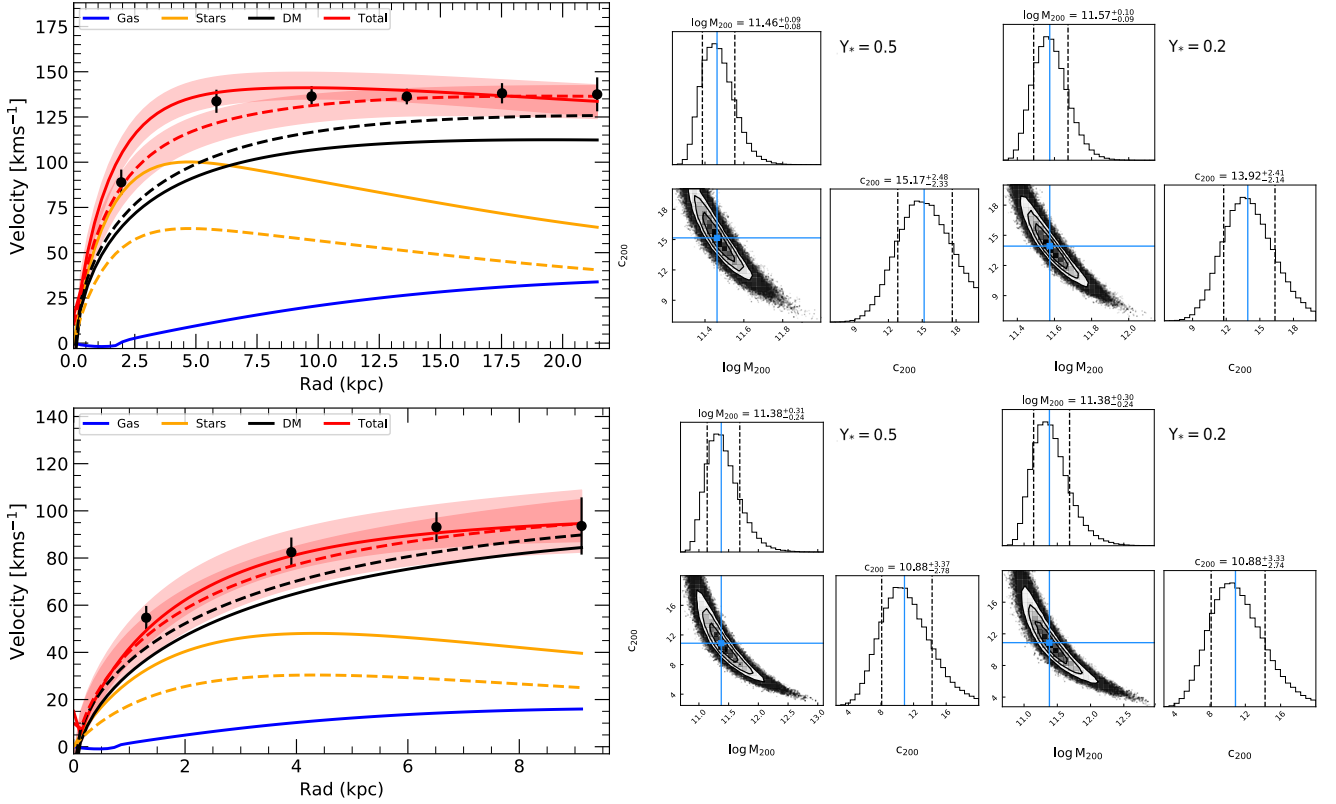


**Figure 8.** Mass modelling of the NFW halo profile for two galaxies J095720.6+015507 and J100211.2+020118. The upper panel shows the rotation curve decomposition for a galaxy with a poly-exponential stellar disc, and the lower panel for a galaxy with a pure exponential disc. The decomposition is shown for fixed  $\Upsilon_*$  values, with solid lines corresponding to  $\Upsilon_* = 0.5$  and dashed lines to  $\Upsilon_* = 0.2$ . The posteriors for these fits are shown on the right.

## 6 DARK MATTER PROPERTIES

Given the limited resolution of the HI rotation curves for our sample, particularly in the inner regions of the galaxies, we only focus on the standard Navarro-Frenk-White (NFW; Navarro et al. 1996) dark matter halo density profile. Therefore, we do not attempt to differentiate between various DM halo models and instead aim to robustly constrain the DM halo mass and assess the position of our sample galaxies with respect to established DM scaling relations. By restricting the complexity of the halo model, we ensure that the inferred parameters are physically motivated. Assuming spherical symmetry, the NFW density profile is defined as:

$$\rho = \frac{4\rho_s}{\left(\frac{r}{r_s}\right)\left(1 + \frac{r}{r_s}\right)^2}, \quad (6)$$

where  $r_s$  is a scale radius, and  $\rho_s$  is the characteristic density at  $r_s$ . The characteristic density  $\rho_s$  is related to the halo mass  $M_{200}$  and concentration  $c_{200}$  as

$$\rho_s = \frac{M_{200}}{16\pi r_s^3 \left[ \ln(1 + c_{200}) - \frac{c_{200}}{1+c_{200}} \right]}, \quad (7)$$

where  $M_{200}$  is the mass enclosed within radius  $R_{200}$ , defined such that the average density inside  $R_{200}$  is 200  $\rho_{\text{crit}}$  (with  $\rho_{\text{crit}}$  the critical density of the Universe), and  $c_{200} \equiv R_{200}/r_s$  is the concentration parameter. The enclosed mass at radius  $r$  for an NFW halo can then be expressed through the di-

mensionless variable  $x = r/r_s$ :

$$M(r) = M_{200} \frac{\ln(1+x) - \frac{x}{1+x}}{\ln(1+c_{200}) - \frac{c_{200}}{1+c_{200}}}. \quad (8)$$

Following the notion of spherical symmetry, the circular velocity at radius  $r$  is defined by  $V_{\text{NFW}}(r) = \sqrt{GM(r)/r}$ . Introducing the characteristic velocity  $V_{200} = \sqrt{GM_{200}/R_{200}}$ , we can rewrite  $V_{\text{NFW}}(r)$  in terms of  $c_{200}$  and  $x$ :

$$V_{\text{NFW}}(r) = V_{200} \sqrt{\frac{c_{200}}{x}} \frac{\sqrt{\ln(1+x) - \frac{x}{1+x}}}{\sqrt{\ln(1+c_{200}) - \frac{c_{200}}{1+c_{200}}}}. \quad (9)$$

The total (baryons and DM) circular velocity of a galaxy at each radius is then:

$$V_{\text{tot}}^2(R) = V_{\text{NFW}}^2(R) + V_{\text{disc}}^2(R) + V_{\text{gas}}^2(R), \quad (10)$$

To calculate  $V_{\text{tot}}$  we adopt a standard Bayesian mass-modelling framework combined with Markov Chain Monte Carlo (MCMC) sampling (Posti et al. 2019; Mancera Piña et al. 2022b; Di Teodoro et al. 2023), using the Python implementation *emcee* (Foreman-Mackey et al. 2013). By employing an MCMC sampler, we explore the parameter space defined by halo mass ( $M_{200}$ ) and halo concentration ( $c_{200}$ ). Our goal is to constrain these key parameters by fitting theoretical rotation curves to the observed galaxy kinematics. We assume a  $\Lambda$ CDM cosmology and adopt standard values for the critical density ( $\rho_{\text{crit}}$ ) and gravitational constant ( $G$ ).

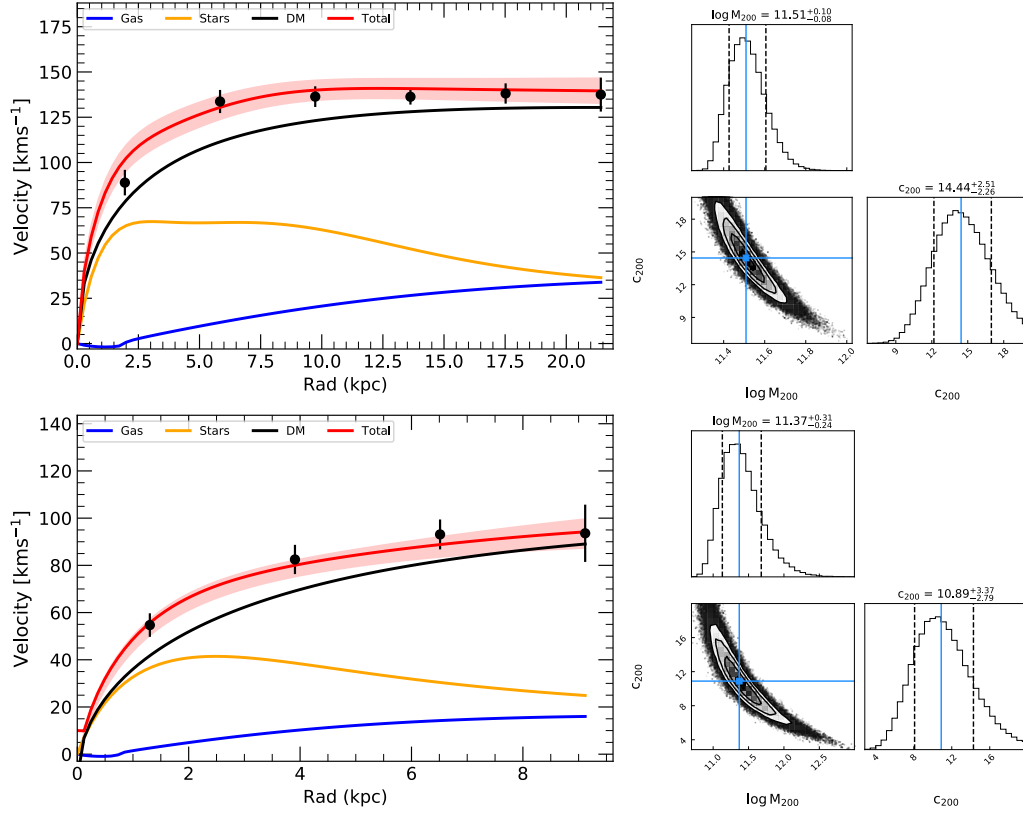


**Figure 9.** Mass modelling of the NFW halo profile for two galaxies J095720.6+015507 and J100211.2+020118 using the resolved stellar surface mass density. The upper panel shows the rotation curve decomposition for a galaxy with a poly-exponential stellar disc, and the lower panel for a galaxy with a pure exponential disc. The posteriors for these fits are shown on the right.

We use a standard  $\chi^2$  likelihood function  $\mathcal{L}$ , defined as:

$$\chi^2 = -2 \ln \mathcal{L}(V_{\text{rot}} | V_{\text{mod}}(x)) = \sum_{i=1}^N \left( \frac{V_{\text{rot}}(r_i) - V_{\text{mod}}(r_i)}{\Delta_i} \right)^2, \quad (11)$$

where  $V_{\text{rot}}(r_i)$  and  $V_{\text{mod}}(r_i)$  are the observed and modelled circular velocities at the  $i$ -th radius  $r_i$ , respectively, and  $\Delta_i$  are the uncertainties on the rotation velocity (Di Teodoro et al. 2023).

We impose physically motivated priors on the fitted parameters during the MCMC sampling. For  $M_{200}$  we use a uniform prior over a wide range  $6 < \log(M_h/M_\odot) \leq 15$ . For the halo concentration instead, we use a lognormal prior based on the mass-concentration relation derived from simulations, enforcing that  $\log_{10}(c_{200})$  follows a normal distribution with a mass-dependent mean and a fixed standard deviation of 0.11 dex (Dutton & Macciò 2014). This choice is motivated by the studies of Katz et al. (2017); Posti et al. (2019), who have shown that even with high-quality local data a strong non-uniform prior on  $c_{200}$  is necessary to obtain proper constraints on the DM halo parameters (but see also Mancera Piña et al. 2022b). Indeed, in Cold Dark Matter (CDM) cosmological simulations, the halo concentration  $c_{200}$  is not independent of  $M_{200}$ . Instead, there is a well-known mass-concentration relation, typically showing that higher-mass halos tend to have lower concentrations. This anti-correlation arises from the formation history of halos. Less massive halos typically

collapse earlier, when the mean background density is higher. Early collapse leads to denser central regions and thus higher concentrations. More massive halos, on the other hand, often form later through mergers and the accretion of matter from a lower-density environment. As a result, their central regions are less compact, resulting in lower concentrations. This relation encodes information about the formation epoch and assembly history of halos, showing that their structure cannot be understood as simple scaled versions of one another (Ludlow et al. 2014; Dutton & Macciò 2014; Diemer & Joyce 2019).

For each fitting run we used 100 walkers for 5000 steps, discarding the first 20% as a burn-in phase. We verify that our fits have converged by computing the integrated autocorrelation time  $\tau$  and ensuring that each walker contributes at least  $50\tau$  samples. Each fitted parameter's central value was taken as the median of its posterior (50th percentile), and uncertainties were defined by the 16th and 84th percentiles. We perform three modelling runs for each galaxy, one with resolved  $\Upsilon_*$ , and another two with  $\Upsilon_*$  fixed at values of 0.2 and 0.5, as described in Section 5.

To assess the quality of the fit and model complexity, we use the Bayesian Information Criterion (BIC):

$$\text{BIC} = -2 \ln(\hat{\mathcal{L}}) + k \ln(n) \quad (12)$$

where  $\hat{\mathcal{L}}$  is the maximum value of the likelihood function for the model,  $k$  is the number of free parameters and  $n$  is the

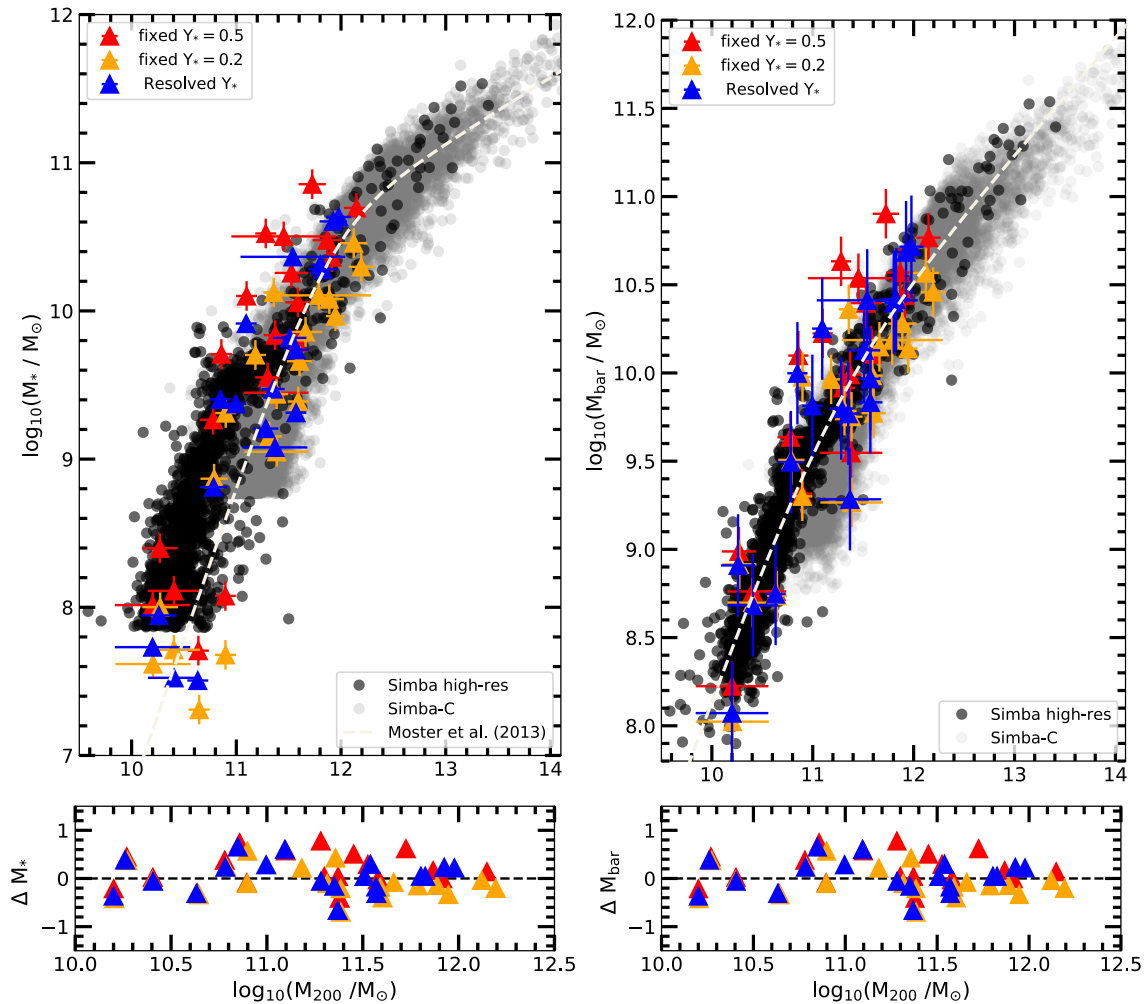


**Figure 10.** Left: Stellar-to-halo mass relation (SHMR) for our sample galaxies derived under different  $\Upsilon_*$  assumptions. Red triangles indicate results obtained with fixed  $\Upsilon_* = 0.5$ , orange symbols correspond to fixed  $\Upsilon_* = 0.2$ , and blue symbols represent models where  $\Upsilon_*$  is left free. Predictions from the SIMBA-C cosmological hydrodynamical simulations are shown as grey points, while the SIMBA high-resolution run is represented by black points. The abundance-matching relation from [Moster et al. \(2013\)](#) is shown as the dashed white line. Right: Baryonic-to-halo mass relation (BHMR) for the same sample. The dashed white line indicates the fitted relation to the theoretical models. The lower panels show the residuals with respect to the corresponding theoretical relations.

number of data points. The BIC provides a means to compare different models and assumptions about the most suitable  $\Upsilon_*$ .

The results for two representative galaxies using  $\Upsilon_* = 0.5$  and  $\Upsilon_* = 0.2$  are shown in Figure 8. The figure presents the rotation-curve decomposition, alongside the posterior distributions of the fitted parameters. The  $M_{200}$  and  $c_{200}$  parameters are tightly constrained, with the posterior distribution of the latter reflecting the imposed mass-concentration relation. This indicates that the dark-matter halo properties are well constrained by the data, largely independently of the adopted stellar mass-to-light ratio. The BIC generally favours the models with  $\Upsilon_* = 0.5$ , with  $\langle \text{BIC}_{0.5} - \text{BIC}_{0.2} \rangle = -29$  ([Kass & Raftery 1995](#)). From Figure 8, it is clear that the main difference between the total rotation curves obtained using the two different  $\Upsilon_*$  values is confined to the central regions of the galaxies. At larger radii, the models converge and therefore reproduce the outer rotation velocities equally well, demonstrating that uncertainties in the stellar mass pre-

scription primarily affect the inner mass distribution, while the outer rotation curve is dominated by the halo.

Figure 9 shows the same rotation-curve decomposition for the same galaxies, but using resolved stellar surface mass density profiles rather than the IRAC 1 surface-brightness profiles scaled by a fixed  $\Upsilon_*$ . Overall, model comparison based on the BIC shows a strong preference for the resolved- $\Upsilon_*$  prescription, with mean offsets of  $\langle \text{BIC}_{\text{resolved}} - \text{BIC}_{0.2} \rangle = -47$  and  $\langle \text{BIC}_{\text{resolved}} - \text{BIC}_{0.5} \rangle = -15$ . From Figure 9 (upper panel), we can see that the model reproduces the observed rotation curve and its features more accurately when the resolved stellar mass surface density is used, with  $\text{BIC}_{\text{resolved}} = 597$ , compared to  $\text{BIC}_{0.5} = 658$  and  $\text{BIC}_{0.2} = 834$ . This improvement reflects the ability of the resolved stellar mass distribution to capture radial variations in the stellar contribution, rather than simply rescaling a fixed light profile, and demonstrates that incorporating spatially resolved stellar mass information leads to a more accurate description of the observed rotation curve, although we note that the best-fit

parameters for  $M_{200}$  and  $c_{200}$  are formally consistent across all tested values of  $\Upsilon_*$ . The  $M_{200}$  obtained using different  $\Upsilon_*$  prescriptions are listed in Table A2.

### 6.1 Halo mass scaling relations

Having derived the halo masses from our rotation curve decompositions, we now examine how these halos relate to their stellar and baryonic content. By combining our halo mass estimates with stellar masses, we first explore the stellar-to-halo mass relation (SHMR). The SHMR describes how the stellar mass of galaxies is connected to the mass of their surrounding DM halo. In essence, it quantifies the efficiency with which baryonic matter is converted into stars at different halo mass scales. Lower-mass halos tend to be less efficient at forming stars (e.g. [Posti et al. 2019](#); [Mancera Piña et al. 2025](#)), presumably due to a combination of factors such as supernova feedback and reionization, while intermediate-mass halos are often thought to be most efficient, and very massive halos may again show reduced star formation efficiency, potentially due to active galactic nuclei feedback and virial shock heating ([Vale & Ostriker 2008](#); [Conroy & Wechsler 2009](#); [Moster et al. 2010](#)). In theoretical work, the SHMR is usually derived via abundance matching (AM) between stellar mass functions and dark matter-only simulations ([Moster et al. 2013](#); [Behroozi et al. 2013, 2019](#)), while observational analyses test whether these relations hold for real galaxies ([Posti et al. 2019](#); [Di Teodoro et al. 2023](#)). These studies highlight the importance of feedback processes and environmental effects in shaping the interplay between dark matter and baryons. The SHMR, therefore, links the growth of stellar mass in galaxies to the assembly of their dark matter halos, providing critical tests for theoretical models of galaxy formation and evolution.

Figure 10 (left) illustrates the SHMR for our sample, computed under three different assumptions for the stellar mass. We quantify the impact of different stellar-mass prescriptions on the inferred halo mass by performing object-by-object comparisons of halo masses obtained from rotation-curve decomposition for the same galaxies, and by characterising the resulting differences through their median offsets and dispersion. Comparing the two fixed mass-to-light ratio prescriptions ( $\Upsilon_* = 0.5$  and  $\Upsilon_* = 0.2$ ) provides a direct measure of the classical disk-halo degeneracy: increasing the stellar mass through a higher global  $\Upsilon_*$  leads to a systematic, although weak, decrease in the inferred halo mass. In our sample, a change of  $\sim 0.4$  dex in stellar mass corresponds to a median decrease of  $\sim 0.05$  dex in  $M_{200}$ , with this inverse trend present across the galaxy population, demonstrating that while the inner mass decomposition remains degenerate, the total halo mass is only weakly sensitive to even extreme assumptions about the global stellar mass-to-light ratio.

The behaviour changes when adopting spatially resolved stellar-mass distributions. In this case, despite a systematic reduction in stellar mass, the inferred halo masses do not show a coherent decrease relative to the fixed- $\Upsilon_*$  models. Instead, the median shift in  $M_{200}$  is small ( $\sim 0.01$  dex), more than an order of magnitude smaller than the intrinsic object-to-object scatter ( $\sim 0.08$  dex), indicating that the differences are dominated by galaxy-to-galaxy variation rather than a population-level offset. This demonstrates that allowing  $\Upsilon_*$  to vary with radius does not result in a simple global trade-off

	Med $\Delta$		$\sigma$	
	$M_*$	$M_{bar}$	$M_*$	$M_{bar}$
$\Upsilon_* = 0.5$	+0.39	+0.09	0.51	0.33
$\Upsilon_* = 0.2$	-0.15	-0.12	0.48	0.30
Resolved $\Upsilon_*$	+0.08	0.04	0.43	0.29

**Table 1.** Table summarising the median offsets ( $\Delta$ ) from the theoretical SHMR and BHMR relations for our sample under different  $\Upsilon_*$  assumptions (Figure 10), along with the observed scatter ( $\sigma$ ) relative to the theoretical relations. All values are expressed in dex.

between stellar and halo components, but instead introduces galaxy-specific responses that lead to a non-uniform impact on the inferred halo mass.

To assess which stellar-mass prescription is most consistent with theoretical expectations, we compare the three samples to the stellar-halo mass relation of [Moster et al. \(2013\)](#) by evaluating the residuals in  $\log M_*$  at fixed  $M_{200}$ . The fixed  $\Upsilon_* = 0.5$  sample lies systematically above the relation, with a median offset of +0.39 dex, while the fixed  $\Upsilon_* = 0.2$  sample lies below it, with a median offset of  $-0.15$  dex. In contrast, the sample based on spatially resolved stellar-mass distributions is much more closely aligned with the theoretical relation, exhibiting a median offset of only +0.08 dex. This offset is smaller in magnitude than for either fixed- $\Upsilon_*$  case and is comparable to the intrinsic scatter of the relation, indicating that the resolved- $\Upsilon_*$  prescription yields stellar-halo mass measurements that are most consistent with the canonical abundance-matching expectation. For visualisation purposes, we also include data from the hydrodynamic cosmological simulations SIMBA (SIMBA-C and high resolution run; [Davé et al. 2019](#)), which show overall consistency with the abundance-matching relation of [Moster et al. \(2013\)](#) across the considered mass range (Figure 10, left).

Incorporating HI gas mass measurements, we also construct the baryonic-to-halo mass relation (BHMR). BHMR extends the concept of the SHMR by considering not only the stellar mass but also the cold gas mass ( $M_* + 1.4 M_{HI}$ ) to form a more complete picture of a galaxy’s total baryon content relative to its host halo. While the SHMR focuses on the efficiency of converting baryons into stars, the baryonic mass-to-halo mass relation captures both the accumulation and retention of baryons, as well as their conversion into stars. By examining the baryonic content, rather than just the stellar component, we can gain insight into how efficient galaxies are at acquiring gas, how much of that gas is converted into stars, and how much is lost through outflows ([Papastergis et al. 2012](#); [McGaugh & Schombert 2015](#); [Mancera Piña et al. 2025](#)).

Figure 10 (right) presents the BHMR for our sample under the three  $\Upsilon_*$  assumptions, alongside the BHMR derived from the SIMBA cosmological simulations. From SIMBA we consider two runs: the ‘flagship’ 100 Mpc/ $h$  box run (minimum stellar mass resolution of  $5.85 \times 10^8 M_\odot$  for all galaxies considered) from the recently updated SIMBA-C simulation ([Hough et al. 2023](#)), which incorporates improved chemical enrichment models, and a high-resolution SIMBA run designed to resolve low-mass galaxies (minimum stellar mass resolution of  $7.30 \times 10^7 M_\odot$ ), similar to those in our sample. We limit the comparison to central galaxies, rather than including satellites to better match the MIGHTEE-HI sample.

As there is no established reference relation for the BHMR,

we fit a double power-law relation to the high-resolution SIMBA sample to provide a baseline against which our observational samples can be compared (Figure 10, right). The best-fitting double power-law parameters are  $\log M_1 = 11.17 \pm 0.20$ ,  $\log N = -1.44 \pm 0.03$  ( $N = 0.0364$ ),  $\beta = 0.60 \pm 0.08$ , and  $\gamma = 0.34 \pm 0.07$ , where  $M_1$  is the characteristic halo mass at which the relation transitions between the low- and high-mass regimes,  $N$  sets the overall normalisation, and  $\beta$  and  $\gamma$  describe the low- and high-mass slopes, respectively. Relative to this relation the sample assuming a fixed  $\Upsilon_* = 0.5$  lies systematically above the fitted relation, with a median offset of  $\sim 0.09$  dex, while the fixed  $\Upsilon_* = 0.2$  sample lies below it, with a median offset of  $\sim 0.12$  dex. In contrast, the sample based on spatially resolved stellar-mass estimates shows the closest agreement, exhibiting a median offset of only  $\sim 0.04$  dex. This behaviour is qualitatively similar to that found for the SHMR AM model, where different stellar-mass assumptions systematically shift galaxies above or below the mean relation, while prescriptions that more accurately capture the stellar mass distribution yield the closest correspondence to the theoretical predictions. It is important to note that several studies have reported deviations from the AM predictions, particularly at high mass scales (Posti et al. 2019; Di Teodoro et al. 2023), but see Desmond & Wechsler (2015); Boreiko et al. (2026) for analyses of how sample selection may impact this. We do not observe such departures within the mass range probed by our sample. This further motivates the use of spatially resolved SED-based mass-to-light ratios in upcoming larger samples. The resulting median offsets and scatter of each sample relative to the theoretical relations are listed in Table 1.

## 7 SUMMARY AND CONCLUSIONS

In this paper, we use deep HI observations from the MIGHTEE survey to derive high-quality HI rotation curves for a sample of 20 galaxies in the COSMOS field across a previously unexplored redshift range,  $0 \leq z \leq 0.08$ . Combining HI rotation curves with carefully derived stellar surface brightness profiles from Spitzer IRAC 1 ( $3.6 \mu\text{m}$ ) band data and resolved stellar mass surface densities profiles from Vărașteanu et al. (2025), we explore mass models for our sample galaxies using the rotation curve decomposition technique. We derived DM halo masses by fitting the observed rotation curves with a parametric NFW halo model (Navarro et al. 1996), combined with our baryonic mass profiles. Using a Bayesian Markov Chain Monte Carlo (MCMC) approach, we explored the parameter space to find the best-fitting halo mass and concentration. By decomposing the HI rotation curves into their baryonic and dark matter components, we obtain observational constraints on the DM halo masses of our sample galaxies and investigate how the DM halos connect to their stellar and baryonic content.

Our main results can be summarised as follows:

- Examining the ratio of the baryonic velocity contribution ( $V_{\text{bar}}$ ) to the total observed velocity ( $V_{\text{obs}}$ ) at the characteristic radius  $R_{2.2}$ , we find that adopting a higher stellar mass-to-light ratio ( $\Upsilon_* = 0.5$ ) produces a clear dependence of  $V_{2.2}/V_{\text{obs}}$  on total galaxy luminosity, consistent with previous studies of nearby disc galaxies (Lelli et al. 2016). In this case, more luminous systems approach  $V_{\text{bar}} \approx V_{\text{obs}}$  at

$R_{2.2}$ , indicating an increased relative baryonic contribution in the inner regions. In contrast, this luminosity dependence largely disappears when a lower value of  $\Upsilon_* = 0.2$  is assumed, resulting in an almost flat  $V_{2.2}/V_{\text{obs}}$ -luminosity relation (Figure 7). This demonstrates that the inferred dynamical role of baryons is highly sensitive to the assumed stellar mass-to-light ratio.

Crucially, when resolved stellar mass surface density profiles are used instead of a fixed  $\Upsilon_*$ , the physically meaningful dependence of  $V_{2.2}/V_{\text{obs}}$  on luminosity is preserved, with a slope comparable to that obtained for  $\Upsilon_* = 0.5$ , while avoiding the suppression of this trend seen for  $\Upsilon_* = 0.2$ . This shows that allowing for galaxy-dependent and radially varying stellar mass-to-light ratios provides a more realistic description of the stellar contribution to galaxy dynamics. These results highlight that the disc-halo degeneracy is strongly amplified by the assumption of a universal stellar mass-to-light ratio, and that incorporating resolved stellar mass information offers a more physically motivated framework for interpreting rotation curves in the context of galaxy formation models and the interplay between baryonic and dark matter.

- Comparing rotation-curve decompositions based on fixed and resolved stellar mass prescriptions, we find that differences between models with fixed  $\Upsilon_*$  are confined to the central regions, while the outer rotation curves are reproduced equally well, indicating that uncertainties in the stellar mass primarily affect the inner mass distribution (Figure 8). Using resolved stellar surface mass density profiles yields a statistically preferred description of the data, improving the reproduction of detailed rotation-curve features (Figure 9). This demonstrates that incorporating spatially resolved stellar mass information provides a more accurate and physically motivated representation of galaxy rotation curves than globally scaled light profiles.
- By comparing stellar-halo mass relations derived under different stellar-mass prescriptions, we show that the inferred total halo mass is only weakly sensitive to even extreme assumptions about a global stellar mass-to-light ratio. While fixed- $\Upsilon_*$  models exhibit the expected inverse response between stellar and halo mass, the resulting shifts in  $M_{200}$  are small compared to the intrinsic galaxy-to-galaxy scatter. Adopting spatially resolved stellar-mass distributions further alters this behaviour: variations in stellar mass do not translate into a coherent population-level shift in halo mass, but instead produce galaxy-specific responses in the mass decomposition (Figure 10 left). When compared to the theoretical abundance-matching expectations (Moster et al. 2010), the resolved-stellar-mass case yields the smallest residuals and the closest overall agreement, indicating that allowing for radial variations in the stellar mass provides a more internally consistent mapping between stellar and halo mass than either fixed- $\Upsilon_*$  assumption.
- By incorporating HI gas mass measurements, we extend our analysis to the baryonic-halo mass relation (BHMR), which provides a more complete view of the total baryon content of galaxies relative to their host haloes. Comparing our observational BHMR to SIMBA simulations, we find that different stellar mass-to-light ratio assumptions systematically shift galaxies relative to the simulation-based reference relation: fixed  $\Upsilon_* = 0.5$  places galaxies above the relation, while  $\Upsilon_* = 0.2$  shifts them below it. In contrast, stellar masses derived from spatially resolved measurements yield the small-

est offsets and the closest overall agreement with the fitted SIMBA baseline (Figure 10 right). This behaviour mirrors that observed for the SHMR, indicating that prescriptions which more accurately capture the stellar mass distribution also provide the most consistent mapping between baryonic mass and halo mass, and minimise systematic biases when comparing observations to theoretical predictions.

In conclusion, studies of galaxy rotation curves and mass modelling provide key insights into the nature of dark matter, the distribution of baryonic matter, and the physical processes governing galaxy formation and evolution. With current and forthcoming observational facilities, such as the SKA, extending these analyses to higher redshifts will enable us to trace the evolution of mass distributions over cosmic time, offering stringent tests of cosmological models.

In this paper, we have demonstrated that employing spatially resolved spectral energy distribution (SED) fitting across a broad wavelength range provides a powerful avenue for mitigating the disc–halo degeneracy. By mapping stellar populations and dust content across galaxies, resolved SED modelling yields spatially resolved stellar mass surface density profiles, removing the need to assume a single, global mass-to-light ratio. This multi-wavelength approach, spanning ultraviolet to infrared bands, naturally accounts for variations in stellar population age, metallicity, and dust attenuation, all of which have a strong impact on inferred mass-to-light ratios. Incorporating this information into mass modelling leads to a more physically motivated characterisation of the stellar mass distribution and enables a clearer separation between baryonic and dark-matter contributions to galaxy rotation curves.

At the same time, important observational challenges remain. The limited spatial resolution of current HI data beyond the very local universe (Ponomareva et al. 2021), together with the signal-to-noise limitations of large HI surveys (Deg et al. 2024), restrict our ability to probe the gravitational potential in the innermost regions of galaxies. As a result, distinguishing robustly between different dark-matter halo models, such as cored versus cuspy profiles, remains difficult (de Blok & McGaugh 1997; Kurapati et al. 2020; Mancera Piña et al. 2025). Future progress will therefore rely on multi-wavelength synergies, particularly the combination of HI data with high-resolution optical emission-line observations (e.g. H $\alpha$ ) that trace the inner galaxy regions (Di Teodoro et al. 2023). Such joint analyses will improve constraints on the central mass distribution, further reduce modelling degeneracies, and provide stronger tests of dark-matter halo structure.

## ACKNOWLEDGEMENTS

We thank the anonymous referee for helpful comments that significantly improved this paper.

AAP is grateful to Giuliano Iorio for making GALPYNAMICS publicly available and for providing support in its use.

The MeerKAT telescope is operated by the South African Radio Astronomy Observatory, which is a facility of the National Research Foundation, an agency of the Department of Science and Innovation. We acknowledge use of the Inter-University Institute for Data Intensive Astronomy (IDIA) data intensive research cloud for data processing. IDIA is a

South African university partnership involving the University of Cape Town, the University of Pretoria and the University of the Western Cape. The authors acknowledge the Centre for High Performance Computing (CHPC), South Africa, for providing computational resources to this research project.

This work is based in part on archival data obtained with the Spitzer Space Telescope, which was operated by the Jet Propulsion Laboratory, California Institute of Technology under a contract with NASA. Support for this work was provided by an award issued by JPL/Caltech.

This work is based in part on data products produced at Terapix available at the Canadian Astronomy Data Centre as part of the Canada-France-Hawaii Telescope Legacy Survey, a collaborative project of NRC and CNRS. The Hyper SuprimeCam (HSC) collaboration includes the astronomical communities of Japan and Taiwan, and Princeton University. The HSC instrumentation and software were developed by the National Astronomical Observatory of Japan (NAOJ), the Kavli Institute for the Physics and Mathematics of the Universe (Kavli IPMU), the University of Tokyo, the High Energy Accelerator Research Organization (KEK), the Academia Sinica Institute for Astronomy and Astrophysics in Taiwan (ASIAA), and Princeton University. Funding was contributed by the FIRST program from Japanese Cabinet Office, the Ministry of Education, Culture, Sports, Science and Technology (MEXT), the Japan Society for the Promotion of Science (JSPS), Japan Science and Technology Agency (JST), the Toray Science Foundation, NAOJ, Kavli IPMU, KEK, ASIAA, and Princeton University.

AAP, MJJ and IH acknowledge support of the STFC consolidated grant ST/S000488/1. MJJ, IH, AV, TY, HP and SK acknowledge the support of a UKRI Frontiers Research Grant [EP/X026639/1], which was selected by the European Research Council. MJJ and AAP acknowledge support from the Oxford Hintze Centre for Astrophysical Surveys, which is funded through generous support from the Hintze Family Charitable Foundation. PEMP acknowledges the support from the Dutch Research Council (NWO) through the Veni grant VI.Veni.222.364. IH acknowledges support from the South African Radio Astronomy Observatory (SARAO) which is a facility of the National Research Foundation (NRF), an agency of the Department of Science and Innovation. MG is supported by the UK STFC Grant ST/Y001117/1. MG acknowledges support from the Inter-University Institute for Data Intensive Astronomy (IDIA). HD is supported by a Royal Society University Research Fellowship (grant no. 211046). KAO acknowledges support by the Royal Society through a Dorothy Hodgkin Fellowship (DHF/R1/231105). IP acknowledges support from the Italian Ministry of Foreign Affairs and International Cooperation (grant number PGR ZA23GR03) and from INAF under the Large Grant 2022 funding scheme (project "MeerKAT and LOFAR Team up: a Unique Radio Window on Galaxy/AGN co-Evolution"). M.B. and A.G. gratefully acknowledge the financial support from the Flemish Fund for Scientific Research (FWO-Vlaanderen) and the South African National Research Foundation (NRF) under their Bilateral Scientific Cooperation program (grant G0G0420N). They also acknowledge the support of networking activities by NRF and the Belgian Science Policy Office (BELSPO), under grant BL/02/SA12 (GALSIMAS).

For the purpose of open access, the author has applied a

Creative Commons Attribution (CC BY) licence to any Author Accepted Manuscript version arising from this submission.

This research has made use of NASA’s Astrophysics Data System Bibliographic Services. This research made use of Astropy<sup>3</sup>, a community-developed core Python package for Astronomy.

## DATA AVAILABILITY

The raw visibility data are publicly available from the SARAO archive by searching for the capture block IDs listed in Table 1 of Heywood et al. (2024). The Spitzer IRAC 1 images used in this work are also publicly accessible as part of S-COSMOS (Sanders et al. 2007). Tables summarising the main properties of the sample and the derived parameters are provided in the Appendix (Tables A1 and A2). All data involved in the analysis are available upon reasonable request to the corresponding author.

## REFERENCES

- Aihara H., et al., 2018, *PASJ*, **70**, S4  
 Aihara H., et al., 2019, *PASJ*, **71**, 114  
 Allaert F., Gentile G., Baes M., 2017, *A&A*, **605**, A55  
 Aniyani S., et al., 2018, *MNRAS*, **476**, 1909  
 Aniyani S., Ponomareva A. A., Freeman K. C., Arnaboldi M., Gerhard O. E., Coccato L., Kuijken K., Merrifield M., 2021, *MNRAS*, **500**, 3579  
 Arnett D., 1999, *Ap&SS*, **265**, 29  
 Bacchini C., Fraternali F., Iorio G., Pezzulli G., 2019, *A&A*, **622**, A64  
 Balmaverde B., et al., 2021, *A&A*, **645**, A12  
 Begeman K. G., 1989, *A&A*, **223**, 47  
 Begeman K. G., Broeils A. H., Sanders R. H., 1991, *MNRAS*, **249**, 523  
 Behroozi P. S., Wechsler R. H., Conroy C., 2013, *ApJ*, **770**, 57  
 Behroozi P., Wechsler R. H., Hearin A. P., Conroy C., 2019, *MNRAS*, **488**, 3143  
 Bershady M. A., Verheijen M. A. W., Swaters R. A., Andersen D. R., Westfall K. B., Martinsson T., 2010, *ApJ*, **716**, 198  
 Binney J., Tremaine S., 2008, *Galactic Dynamics*, 2 edn. Princeton University Press, Princeton, NJ  
 Boreiko F., Yasin T., Desmond H., Stiskalek R., Jarvis M. J., 2026, *arXiv e-prints*, p. arXiv:2601.07799  
 Bosma A., 1978, PhD thesis, University of Groningen, Netherlands  
 Bosma A., 1981, *AJ*, **86**, 1825  
 Ciotti L., Bertin G., 1999, *A&A*, **352**, 447  
 Combes F., et al., 2019, *A&A*, **623**, A79  
 Comerón S., Salo H., Knapen J. H., 2018, *A&A*, **610**, A5  
 Conroy C., Wechsler R. H., 2009, *ApJ*, **696**, 620  
 Davé R., Anglés-Alcázar D., Narayanan D., Li Q., Rafieferantsoa M. H., Appleby S., 2019, *MNRAS*, **486**, 2827  
 Deg N., et al., 2022, *Publ. Astron. Soc. Australia*, **39**, e059  
 Deg N., et al., 2024, *arXiv e-prints*, p. arXiv:2411.06993  
 Desmond H., Wechsler R. H., 2015, *MNRAS*, **454**, 322  
 Di Cintio A., Lelli F., 2016, *MNRAS*, **456**, L127  
 Di Cintio A., Brook C. B., Dutton A. A., Macciò A. V., Stinson G. S., Knebe A., 2014, *MNRAS*, **441**, 2986  
 Di Teodoro E. M., Fraternali F., 2015, *MNRAS*, **451**, 3021  
 Di Teodoro E. M., et al., 2023, *MNRAS*, **518**, 6340  
 Diemer B., Joyce M., 2019, *ApJ*, **871**, 168  
 Dutton A. A., Macciò A. V., 2014, *MNRAS*, **441**, 3359  
 Foreman-Mackey D., Hogg D. W., Lang D., Goodman J., 2013, *PASP*, **125**, 306  
 Fouque P., Bottinelli L., Gouguenheim L., Patrel G., 1990, *ApJ*, **349**, 1  
 Frank B. S., de Blok W. J. G., Walter F., Leroy A., Carignan C., 2016, *AJ*, **151**, 94  
 Freeman K. C., 1970, *ApJ*, **160**, 811  
 Heald G., et al., 2011, *A&A*, **526**, A118  
 Heywood I., et al., 2024, *MNRAS*,  
 Hough R. T., Rennehan D., Kobayashi C., Loubser S. I., Davé R., Babul A., Cui W., 2023, *MNRAS*, **525**, 1061  
 Howell S. B., 2006, *Handbook of CCD Astronomy*, 2 edn. Cambridge Observing Handbooks for Research Astronomers Vol. 5, Cambridge University Press  
 Ianjamasimanana R., de Blok W. J. G., Walter F., Heald G. H., Caldú-Primo A., Jarrett T. H., 2015, *AJ*, **150**, 47  
 Iorio G., Fraternali F., Nipoti C., Di Teodoro E., Read J. I., Battaglia G., 2017, *MNRAS*, **466**, 4159  
 Jarvis M. J., et al., 2013, *MNRAS*, **428**, 1281  
 Jarvis M., et al., 2016, in *MeerKAT Science: On the Pathway to the SKA*. p. 6 ([arXiv:1709.01901](https://arxiv.org/abs/1709.01901))  
 Jonas J. L., 2009, *IEEE Proceedings*, **97**, 1522  
 Kamphuis P., Józsa G. I. G., Oh S. H., Spekkens K., Urbancic N., Serra P., Koribalski B. S., Dettmar R. J., 2015, *MNRAS*, **452**, 3139  
 Kass R. E., Raftery A. E., 1995, *Journal of the American Statistical Association*, **90**, 773  
 Katz H., Lelli F., McGaugh S. S., Di Cintio A., Brook C. B., Schombert J. M., 2017, *MNRAS*, **466**, 1648  
 Klypin A. A., Trujillo-Gomez S., Primack J., 2011, *ApJ*, **740**, 102  
 Kormendy J., Kennicutt Robert C. J., 2004, *ARA&A*, **42**, 603  
 Kurapati S., Chengalur J. N., Kamphuis P., Pustilnik S., 2020, *MNRAS*, **491**, 4993  
 Lelli F., McGaugh S. S., Schombert J. M., 2016, *AJ*, **152**, 157  
 Ludlow A. D., Navarro J. F., Angulo R. E., Boylan-Kolchin M., Springel V., Frenk C., White S. D. M., 2014, *MNRAS*, **441**, 378  
 Maddox N., et al., 2021, *A&A*, **646**, A35  
 Mancera Piña P. E., et al., 2020, *MNRAS*, **495**, 3636  
 Mancera Piña P. E., Posti L., Fraternali F., Adams E. A. K., Oosterloo T., 2021, *A&A*, **647**, A76  
 Mancera Piña P. E., Fraternali F., Oosterloo T., Adams E. A. K., Oman K. A., Leisman L., 2022a, *MNRAS*, **512**, 3230  
 Mancera Piña P. E., Fraternali F., Oosterloo T., Adams E. A. K., di Teodoro E., Bacchini C., Iorio G., 2022b, *MNRAS*, **514**, 3329  
 Mancera Piña P. E., Golini G., Trujillo I., Montes M., 2024, *A&A*, **689**, A344  
 Mancera Piña P. E., Read J. I., Kim S., Marasco A., Benavides J. A., Glowacki M., Pezzulli G., Lagos C. d. P., 2025, *A&A*, **699**, A311  
 Mancera Piña P. E., Di Teodoro E. M., Fall S. M., Marasco A., Kriek M., Martorano M., 2026, *A&A*, **705**, A180  
 Marasco A., Posti L., Oman K., Famaey B., Cresci G., Fraternali F., 2020, *A&A*, **640**, A70  
 Marasco A., et al., 2023, *A&A*, **670**, A92  
 Marasco A., Fall S. M., Di Teodoro E. M., Mancera Piña P. E., 2025, *A&A*, **695**, L23  
 Martinsson T. P. K., Verheijen M. A. W., Westfall K. B., Bershady M. A., Andersen D. R., Swaters R. A., 2013, *A&A*, **557**, A131  
 Martinsson T. P. K., Verheijen M. A. W., Bershady M. A., Westfall K. B., Andersen D. R., Swaters R. A., 2016, *A&A*, **585**, A99  
 McCracken H. J., et al., 2012, *A&A*, **544**, A156  
 McGaugh S. S., Schombert J. M., 2014, *AJ*, **148**, 77  
 McGaugh S. S., Schombert J. M., 2015, *ApJ*, **802**, 18  
 McGaugh S. S., Schombert J. M., Bothun G. D., de Blok W. J. G., 2000, *ApJ*, **533**, L99

<sup>3</sup> <http://www.astropy.org>

- McGaugh S. S., Lelli F., Schombert J. M., 2016, *Physical Review Letters*, **117**, 201101
- Meidt S. E., et al., 2012a, *ApJ*, **744**, 17
- Meidt S. E., et al., 2012b, *ApJ*, **744**, 17
- Meidt S. E., et al., 2014a, *ApJ*, **788**, 144
- Meidt S. E., et al., 2014b, *ApJ*, **788**, 144
- Meyer M., Robotham A., Obreschkow D., Westmeier T., Duffy A. R., Staveley-Smith L., 2017, *Publications of the Astronomical Society of Australia*, **34**
- Mogotsi K. M., de Blok W. J. G., Caldú-Primo A., Walter F., Ianjamasimanana R., Leroy A. K., 2016, *AJ*, **151**, 15
- Moster B. P., Somerville R. S., Maubetsch C., van den Bosch F. C., Macciò A. V., Naab T., Oser L., 2010, *ApJ*, **710**, 903
- Moster B. P., Naab T., White S. D. M., 2013, *MNRAS*, **428**, 3121
- Navarro J. F., Frenk C. S., White S. D. M., 1996, *ApJ*, **462**, 563
- Oh S.-H., et al., 2015, *AJ*, **149**, 180
- Papastergis E., Cattaneo A., Huang S., Giovanelli R., Haynes M. P., 2012, *ApJ*, **759**, 138
- Planck Collaboration et al., 2020, *A&A*, **641**, A6
- Ponomareva A. A., Verheijen M. A. W., Bosma A., 2016, *MNRAS*, **463**, 4052
- Ponomareva A. A., Verheijen M. A. W., Peletier R. F., Bosma A., 2017, *MNRAS*, **469**, 2387
- Ponomareva A. A., Verheijen M. A. W., Papastergis E., Bosma A., Peletier R. F., 2018, *MNRAS*, **474**, 4366
- Ponomareva A. A., et al., 2021, *MNRAS*, **508**, 1195
- Ponomareva A. A., et al., 2023, *MNRAS*, **522**, 5308
- Posti L., Marasco A., Fraternali F., Famaey B., 2019, *A&A*, **629**, A59
- Querejeta M., et al., 2015a, *ApJS*, **219**, 5
- Querejeta M., et al., 2015b, *ApJS*, **219**, 5
- Rajohnson S. H. A., et al., 2022, *MNRAS*, **512**, 2697
- Ranchod S., et al., 2021, *MNRAS*, **506**, 2753
- Read J. I., Iorio G., Agertz O., Fraternali F., 2016a, *MNRAS*, **462**, 3628
- Read J. I., Iorio G., Agertz O., Fraternali F., 2016b, *MNRAS*, **462**, 3628
- Röck B., Vazdekis A., Peletier R. F., Knapen J. H., Falcón-Barroso J., 2015, *MNRAS*, **449**, 2853
- Romeo A. B., 1992, *MNRAS*, **256**, 307
- Rubin V. C., Ford W. K. J., Thonnard N., 1978, *ApJ*, **225**, L107
- Said K., Colless M., Magoulas C., Lucey J. R., Hudson M. J., 2020, *MNRAS*, **497**, 1275
- Sanders D. B., et al., 2007, *ApJS*, **172**, 86
- Schombert J., McGaugh S., Lelli F., 2019, *MNRAS*, **483**, 1496
- Schombert J., McGaugh S., Lelli F., 2022, *AJ*, **163**, 154
- Sheth K., et al., 2010, *PASP*, **122**, 1397
- Springel V., et al., 2005, *Nature*, **435**, 629
- Starkman N., Lelli F., McGaugh S., Schombert J., 2018, *MNRAS*, **480**, 2292
- Swaters R. A., 1999, PhD thesis, University of Groningen, Netherlands
- Tamm A., Tempel E., Tenjes P., Tihhonova O., Tuvikene T., 2012, *A&A*, **546**, A4
- Tollet E., et al., 2016, *MNRAS*, **456**, 3542
- Tonry J. L., Blakeslee J. P., Ajhar E. A., Dressler A., 2000, *ApJ*, **530**, 625
- Tudorache M. N., et al., 2022, *MNRAS*, **513**, 2168
- Tully R. B., Fouque P., 1985, in Richter O. G., Binggeli B., eds, *European Southern Observatory Conference and Workshop Proceedings Vol. 20, European Southern Observatory Conference and Workshop Proceedings*. pp 417–424
- Tully R. B., Courtois H. M., Sorce J. G., 2016, *AJ*, **152**, 50
- Vale A., Ostriker J. P., 2008, *MNRAS*, **383**, 355
- Venturi G., et al., 2021, *A&A*, **648**, A17
- Verheijen M. A. W., 2001, *ApJ*, **563**, 694
- Vărășteanu A. A., et al., 2025, *MNRAS*, **541**, 2366
- Wang J., Koribalski B. S., Serra P., van der Hulst T., Roychowdhury S., Kamphuis P., Chengalur J. N., 2016, *MNRAS*, **460**, 2143
- Yoachim P., Dalcanton J. J., 2006, *AJ*, **131**, 226
- de Blok W. J. G., 2010, *Advances in Astronomy*, **2010**, 789293
- de Blok W. J. G., McGaugh S. S., 1997, *MNRAS*, **290**, 533
- de Blok W. J. G., Walter F., Brinks E., Trachternach C., Oh S. H., Kennicutt R. C. J., 2008, *AJ*, **136**, 2648
- de Blok W. J. G., et al., 2016, *AJ*, **152**, 51
- Šiljeg B., et al., 2024, *A&A*, **692**, A217
- van Albada T. S., Sancisi R., 1986, *Philosophical Transactions of the Royal Society of London Series A*, **320**, 447
- van Albada T. S., Bahcall J. N., Begeman K., Sancisi R., 1985, *ApJ*, **295**, 305
- van der Kruit P. C., Freeman K. C., 2011, *ARA&A*, **49**, 301

## APPENDIX A: SAMPLE DATA TABLES

Tables summarising the main properties of our sample [A1](#) and the results of the mass modelling [A2](#)

Name	ra deg	dec deg	z	$\log_{10}(\text{MHI})$ $M_{\odot}$	$i^{\circ}$ deg	$h_d$ kpc	pa deg	Nb	$\log_{10}(L_{\text{IR1}})$ $L_{\odot}$	$\log_{10}(M_{\star})$ $M_{\odot}$
J095829.1+014139	149.621	1.694	0.006	$9.144 \pm 0.008$	66.759	$1.933 \pm 0.251$	60.752	11	$8.378 \pm 0.137$	–
J095846.8+022051	149.695	2.348	0.006	$8.575 \pm 0.015$	69.235	$1.034 \pm 0.134$	311.745	7	$8.008 \pm 0.133$	$7.485 \pm 0.088$
J095927.9+020025	149.866	2.007	0.013	$8.505 \pm 0.065$	40.824	$0.972 \pm 0.126$	293.299	3	$8.412 \pm 0.137$	$7.653 \pm 0.101$
J100005.8+015440	150.024	1.911	0.006	$7.661 \pm 0.126$	65.857	$0.794 \pm 0.103$	116.527	3	$8.316 \pm 0.136$	$7.823 \pm 0.063$
J095904.3+021516	149.768	2.254	0.025	$8.713 \pm 0.115$	52.729	$1.908 \pm 0.248$	29.397	3	$8.700 \pm 0.130$	$7.985 \pm 0.085$
J100211.2+020118	150.547	2.022	0.021	$8.713 \pm 0.119$	38.652	$1.936 \pm 0.174$	42.384	3	$9.749 \pm 0.087$	$9.181 \pm 0.098$
J100009.3+024247	150.039	2.713	0.033	$9.472 \pm 0.068$	59.051	$3.277 \pm 0.295$	336.929	5	$10.402 \pm 0.094$	$9.493 \pm 0.094$
J100115.2+021823	150.313	2.306	0.028	$9.248 \pm 0.057$	72.663	$3.100 \pm 0.279$	172.713	4	$9.567 \pm 0.086$	$8.792 \pm 0.092$
J095720.6+015507	149.336	1.919	0.032	$9.690 \pm 0.034$	45.168	$4.270 \pm 0.384$	56.609	5	$10.557 \pm 0.096$	$10.101 \pm 0.076$
J100143.2+024109	150.430	2.686	0.047	$9.712 \pm 0.065$	43.408	$3.513 \pm 0.316$	82.713	4	$10.088 \pm 0.091$	$9.433 \pm 0.099$
J100259.0+022035	150.746	2.343	0.044	$9.769 \pm 0.065$	47.931	$4.705 \pm 0.423$	256.795	6	$11.156 \pm 0.102$	$10.921 \pm 0.101$
J100055.2+022344	150.230	2.395	0.044	$9.274 \pm 0.148$	44.149	$2.441 \pm 0.220$	210.507	5	$10.804 \pm 0.098$	$10.531 \pm 0.083$
J095923.2+024137	149.847	2.694	0.048	$8.983 \pm 0.272$	48.236	$3.276 \pm 0.295$	83.175	3	$10.359 \pm 0.094$	$9.753 \pm 0.105$
J100236.5+014836	150.652	1.810	0.046	$9.725 \pm 0.043$	56.564	$5.582 \pm 0.502$	329.657	4	$10.010 \pm 0.090$	$9.474 \pm 0.127$
J100117.1+020337	150.321	2.060	0.062	$9.317 \pm 0.114$	49.847	$3.443 \pm 0.310$	138.907	3	$10.138 \pm 0.091$	$9.505 \pm 0.099$
J100003.9+015253	150.016	1.881	0.065	$9.524 \pm 0.202$	60.666	$3.562 \pm 0.321$	18.422	5	$9.852 \pm 0.089$	$9.194 \pm 0.091$
J095755.9+022608	149.483	2.436	0.071	$9.508 \pm 0.197$	78.558	$6.341 \pm 0.571$	59.042	5	$10.664 \pm 0.097$	$10.081 \pm 0.104$
J100217.9+015124	150.574	1.857	0.062	$9.701 \pm 0.088$	51.440	$3.743 \pm 0.337$	340.661	3	$10.779 \pm 0.098$	$10.312 \pm 0.122$
J100103.7+023053	150.265	2.515	0.072	$9.837 \pm 0.106$	58.864	$6.061 \pm 0.545$	83.189	5	$10.824 \pm 0.098$	$10.093 \pm 0.105$
J095907.8+024213	149.782	2.704	0.079	$9.804 \pm 0.098$	49.830	$8.351 \pm 0.752$	295.425	4	$10.996 \pm 0.100$	$10.814 \pm 0.077$

**Table A1.** Table summarising our sample main properties. Column (1): Galaxy identifier; Column (2): Right ascension of the galaxy in degrees (J2000); Column (3): Declination of the galaxy in degrees (J2000); Column (4): Redshift derived from the HI line; Column (5):  $\log_{10}$  of the galaxy’s HI mass; Column (6): Inclination angle (in degrees), measured from IRAC 1 imaging; Column (7): Stellar disc scale length in kiloparsecs; Column (8): Position angle (in degrees), used for kinematic modelling; Column (9): Number of the resolution elements across the major axis of the HI moment 1 map; Column (10):  $\log_{10}$  of total luminosity in the Spitzer 3.6  $\mu\text{m}$  band; Column (11):  $\log_{10}$  of the galaxy’s stellar mass derived using resolved  $\Upsilon_{\star}$ .

Name	$\log_{10}(M_{200}^{\Upsilon_*=0.5})$ $M_{\odot}$	$\log_{10}(M_{200}^{\Upsilon_*=0.2})$ $M_{\odot}$	$\log_{10}(M_{200}^{\text{SED}\Upsilon_*})$ $M_{\odot}$
J095829.1+014139	$10.895^{+0.10}_{-0.09}$	$10.896^{+0.10}_{-0.09}$	–
J095846.8+022051	$10.638^{+0.10}_{-0.09}$	$10.645^{+0.10}_{-0.09}$	$10.632^{+0.10}_{-0.09}$
J095927.9+020025	$10.405^{+0.24}_{-0.18}$	$10.404^{+0.24}_{-0.18}$	$10.406^{+0.24}_{-0.18}$
J100005.8+015440	$10.201^{+0.35}_{-0.22}$	$10.204^{+0.34}_{-0.23}$	$10.200^{+0.35}_{-0.22}$
J095904.3+021516	$10.269^{+0.17}_{-0.14}$	$10.273^{+0.17}_{-0.14}$	$10.260^{+0.17}_{-0.14}$
J100211.2+020118	$11.431^{+0.08}_{-0.07}$	$11.553^{+0.09}_{-0.08}$	$11.369^{+0.31}_{-0.24}$
J100009.3+024247	$11.098^{+0.08}_{-0.06}$	$11.182^{+0.08}_{-0.07}$	$10.996^{+0.07}_{-0.05}$
J100115.2+021823	$10.780^{+0.13}_{-0.11}$	$10.788^{+0.13}_{-0.11}$	$10.783^{+0.13}_{-0.11}$
J095720.6+015507	$11.166^{+0.20}_{-0.15}$	$11.171^{+0.19}_{-0.15}$	$11.509^{+0.10}_{-0.08}$
J100143.2+024109	$11.578^{+0.10}_{-0.08}$	$11.591^{+0.09}_{-0.08}$	$11.570^{+0.09}_{-0.08}$
J100259.0+022035	$11.725^{+0.12}_{-0.12}$	$12.121^{+0.11}_{-0.09}$	$11.925^{+0.09}_{-0.01}$
J100055.2+022344	$11.453^{+0.29}_{-0.31}$	$11.788^{+0.28}_{-0.25}$	$11.540^{+0.18}_{-0.15}$
J095923.2+024137	$11.588^{+0.11}_{-0.09}$	$11.604^{+0.12}_{-0.10}$	$11.571^{+0.11}_{-0.09}$
J100236.5+014836	$10.858^{+0.09}_{-0.08}$	$10.899^{+0.09}_{-0.08}$	$10.848^{+0.09}_{-0.08}$
J100117.1+020337	$11.371^{+0.12}_{-0.10}$	$11.385^{+0.12}_{-0.10}$	$11.352^{+0.12}_{-0.10}$
J100003.9+015253	$11.299^{+0.08}_{-0.08}$	$11.315^{+0.08}_{-0.08}$	$11.282^{+0.08}_{-0.07}$
J095755.9+022608	$11.914^{+0.09}_{-0.08}$	$11.947^{+0.09}_{-0.08}$	$11.803^{+0.08}_{-0.07}$
J100217.9+015124	$11.867^{+0.14}_{-0.11}$	$11.888^{+0.14}_{-0.12}$	$11.826^{+0.13}_{-0.11}$
J100103.7+023053	$11.281^{+0.10}_{-0.09}$	$11.358^{+0.10}_{-0.09}$	$11.094^{+0.10}_{-0.09}$
J095907.8+024213	$12.148^{+0.12}_{-0.10}$	$12.193^{+0.12}_{-0.11}$	$11.978^{+0.11}_{-0.10}$

**Table A2.** Table summarising the DM halo mass ( $M_{200}$ ) obtained using different assumption of the mass-to-light ratio in mass modelling. Column (1): Galaxy identifier; Column (2):  $M_{200}$  assuming  $\Upsilon_* = 0.5$ ; Column (3):  $M_{200}$  assuming  $\Upsilon_* = 0.2$ ; Column (4):  $M_{200}$  assuming resolved  $\Upsilon_*$